

Overview of pre- and post-processing of ambient-noise correlations

Michael H. Ritzwoller and Lili Feng

Abstract

All applications of ambient seismic noise, whether to study the source of the noise or the medium of propagation (static or time variable), are based fundamentally on a single observational challenge. This challenge is to process raw seismograms in a way that promotes the emergence of the signals of interest while suppressing the signals of disinterest. Here we summarize methods designed to achieve this delicate task in both continental and oceanic settings and review evidence that the observational challenge is met successfully.

5.1 Introduction

The purpose of this chapter is to discuss the problem of how to prepare seismic recordings for ambient noise data processing, and to assess how well cross-correlations of such records summarize information about the Earth. Our focus will be on broad-band seismic data at relatively long periods (5 - 100 s) observed over relatively long distances (a few 10s of km to a few 1000s of km). Such data, recorded on recent-generation broad-band seismic arrays such as USArray, provide information about the Earth with lateral resolutions on a regional scale (i.e., from a few 10s to a few 100s of km). Signals of this nature derived from ambient noise are enriched in fundamental modes, so that most information derived about the Earth relates to the structure of the crust and uppermost mantle. Although our focus is fairly tight, ignoring as it does problems that may be encountered in exploration seismology and the extraction of body waves, which is discussed in Chapter 8 (Nakata and Nishida, 2018), the issues we consider are universal. The problem we address

is how to construct reliable information about the Earth from observations that most of us would think of as noise.

Our approach is practical, heuristic, and non-rigorous. It is not historical and we do not attempt to provide a comprehensive summary of ambient noise pre-and post-processing procedures that have developed over the somewhat more than decade long history of ambient noise seismology. Rather, we aim to provide a discussion that researchers who are interested in pursuing the subject may find useful as a starting point or as a guide to pursue their own creative work in ambient noise seismology.

It is remarkable that seismologists can derive deterministic structural information from recordings of seismic noise. Snieder (2004) provides a lucid and rigorous proof that the cross-correlation of seismograms recorded at a pair of stations will yield the Green's function between the stations, at least in the idealized setting underlying the proof. The Green's function is the impulse response of the medium, and provides structural information about the medium of transport between the stations.

The reader is referred to Chapter 4 (Fichtner and Tsai, 2018) for a more comprehensive discussion of the theory behind the emergence of signals from ambient noise. However, a significant aspect of the idealized setting of the proof referred to in the previous paragraph is that the sources of ambient noise are non-correlated and randomly and homogeneously distributed in space and time. Observing conditions in the earth do not meet these conditions; thus the best that any data processing procedure can achieve is a plausible approximation to the Green's function.

Figure 5.1 motivates a heuristic explanation why Green's functions might emerge approximately in practice from cross-correlations of ambient noise. A hyperbola is defined as the set of points in a plane in which the difference between the distances to two fixed points is a constant k . Figure 5.1 shows a set of hyperbolas where the fixed points are a pair of seismic stations (the two triangles in the figure). Each hyperbola is characterized by a single constant k which differs from its nearest neighbors by $\pm\pi$. Thus, the hyperbolas in Figure 5.1 are a set of level curves for the constants k . The figure illustrates that the level curves become increasingly closely spaced as they diverge from the horizontal; i.e., from the inter-station direction. As a consequence, over most of the plane two closely spaced seismic events will produce waves that arrive at the two stations at different times (or phase, which is time divided by period) unless they lie nearly exactly along one of the hyperbolas, and the phase difference will depend strongly on the relative locations of the events. If such events have similar amplitudes they will have very different expressions in the seismograms recorded at the two stations, and they will therefore

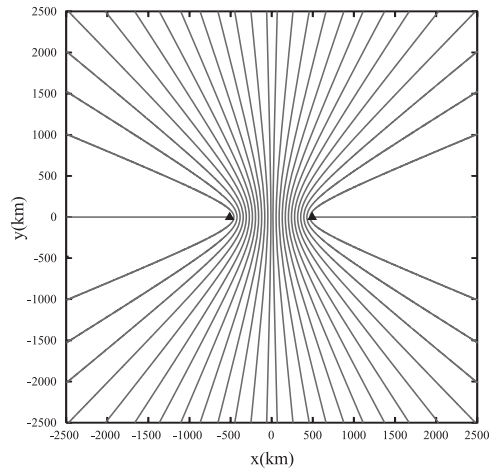


Figure 5.1 Examples of iso-phase hyperbolas (grey lines) in the plane with foci at two stations (triangles) separated from nearest neighbors by $\pm\pi$. A phase speed of 3 km/s at 50 s period is used to compute these hyperbolas. Only sources found on the same hyperbola will constructively interfere on cross-correlations of signals recorded at the two stations. Sources on different hyperbolas will destructively interfere. Sources found near or along the “end-fire” hyperbolas are least likely to be affected by destructively interfering sources, and are therefore most likely to appear on cross-correlations of long time sequences of ambient noise. This figure is adapted from Fig. 16 of Lin et al. (2008).

destructively interfere in the cross-correlation between these seismograms. There are two exceptions to the destructive interference described in the previous paragraph, the first good and the second bad for our purposes.

(1) In the first case, events that are nearly aligned with the two stations (in the so called “end-fire” direction) are more likely to arrive with similar phases on the two recordings because the level curves are more separated from one another. Such events will tend to interfere constructively on cross-correlations. It is this constructive interference between the effects of events nearly aligned with the stations in concert with the destructive interference for events in other directions that results in the recovery of waves propagating between the two stations in the cross-correlation, as long as sufficient numbers of events have taken place. As discussed in section 2, in this case the cross-correlation will be related to the Green’s function between the pair of stations as long as there are events near the end-fire direction and if the duration of observation is long enough.

(2) The second case is a pernicious one, however, in which either an enormous event (with a much larger amplitude than other interfering sources) has

occurred or a series of smaller events occur persistently at a single location. In this case the arrivals will not destructively interfere upon cross-correlation between recordings from the two stations and an interfering signal will remain that is not related to the Green's function between the stations. Examples of such events are the Gulf of Guinea microseism (e.g., Shapiro et al., 2006), also referred to as the 26 s microseism, and the Kyushu microseism (Zeng and Ni, 2010) that results from Aso Volcano, the effects of which have been observed clearly in ambient noise correlations for stations in East Asia (Zheng et al., 2011).

This chapter discusses observational techniques that have emerged to help extract clear estimated (or empirical) Green's functions (EGFs), while discriminating against sources of noise such as earthquakes or persistent localized events. Applications of the estimated Green's functions are discussed in Chapter 7 (Shapiro, 2018). An example of one such estimated Green's function produced from a year of continuous recordings observed at broadband stations HRV and ANMO is shown in Figure 5.2 separated into different frequency bands. Records such as this are sought to form the basis for ambient noise tomography.

There are intermediate circumstances between those that deliver clear estimated Green's functions and those that generate clear artificial arrivals. These are characterized by an azimuthally inhomogeneous source distribution, which is stronger in some directions than others. Many studies have considered whether such situations, which are common in nature, will deliver reliable estimated Green's functions and find that as long as there are events in the end-fire direction, then a reliable estimated Green's functions will emerge eventually (e.g., Lin et al., 2008; Yang and Ritzwoller, 2008); it is just a matter of observing long enough. But, how does an observer know if enough time has elapsed so that a meaningful estimate of the Green's function has emerged? This is one of the principal practical concerns in ambient noise seismology. Another way to ask the same question is: has enough signal emerged from the noise to be useful?

There is no definitive answer to these questions, but there are many relevant indicators as discussed later in section 6. We mention now one line of evidence that is particularly important, related to so-called precursory noise. The time of arrival of a signal on a cross-correlation will be the difference in arrival times from recorded at the two stations. Events on the perpendicular bisector of the line linking the two stations will produce arrivals at the same time on the two stations, and thus will arrive at zero lag time on the cross-correlation. In contrast, events in the end-fire configuration will generate arrivals that are separated by the phase propagation time be-

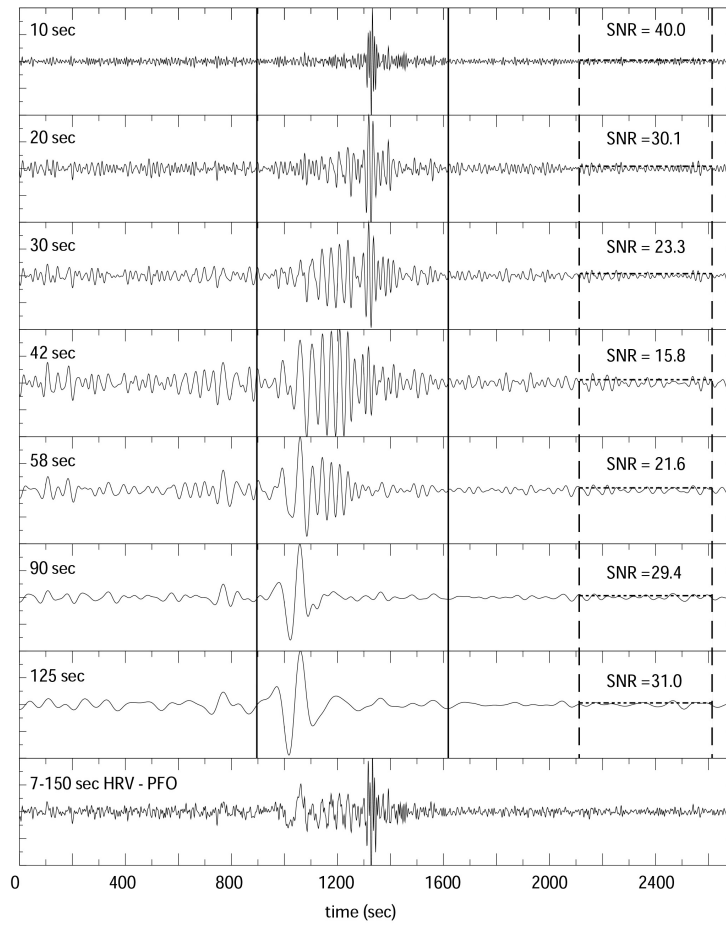


Figure 5.2 Example of a broad-band symmetric-component cross-correlation of 12 months of ambient noise from stations ANMO (Albuquerque, NM, USA) and HRV (Harvard, MA, USA). The broad-band signal is at bottom and successively longer period passbands are presented from top to bottom in the figure, centered on the period shown at left in each panel. Vertical solid lines indicate the signal window and the vertical dashed lines the noise windows. SNR is defined as the peak amplitude in the signal window divided by the amplitude in the trailing noise window (indicated with the horizontal dashed line on each panel). SNR is labeled on the right hand side of each panel. The symmetric-component is the average of the cross-correlations at positive and negative lags, given by equation (5.8). (This figure is taken from Fig. 11 of Bensen et al. (2007)).

tween the two stations. Thus, end-fire events, which constructively interfere to produce the estimated Green’s functions, produce the latest arrivals on the cross-correlation. All other events will produce signals that arrive sooner

and will superpose in the cross-correlation to produce precursory noise. The level of this precursory noise compared to the amplitude of the signal of interest is a good indicator of the convergence of the method toward a reliable estimated Green's function. Some researchers have used the observation of precursors to locate locally persistent sources (e.g., Tian and Ritzwoller, 2015). We take up the issue of precursory noise again in section 6.

This chapter is structured as follows. In section 2 we present the notation and terminology used throughout the chapter and discuss ambient noise data processing in a generalized form. In the end, we seek observational methods to yield broadband, low variance, and unbiased information about the Earth. In addition, we seek methods that will speed convergence and thus reduce observation time. With these goals in mind, sections 3 and 4 discuss the practical and specific application of ambient noise data processing in a continental setting for Rayleigh and Love waves and section 5 presents a discussion of the data processing in ocean bottom environments. Section 6 discusses what might be referred to as post-processing assessment: how do we select some recordings to accept and others to reject (because not all will reflect Earth structure accurately), how do we quantify uncertainties in surface wave dispersion measurements and dispersion maps, and how do we know if our results, in the end, are right? The chapter closes with section 7 in which we present a few examples of new methods that show promise to improve the output from ambient noise data processing.

5.2 Idealized background

Let the vector $\mathbf{u} = (u, v, w)$ be ground motion recorded at an unspecified location, such that u is the vertical component (Z) and v and w are the two horizontal components (east, E, and north, N, respectively). Then let $u_i(t)$ and $u_j(t)$ denote vertical component seismograms at stations i and j separated by distance r , recorded on a finite time interval $t \in [0, T]$. The cross-spectrum between these recordings (or the cross-correlation in the frequency domain) is as follows:

$$\gamma_{ij}(\omega) \equiv u_i(\omega)u_j^*(\omega), \quad (5.1)$$

where $u(\omega)$ is the Fourier Transform of $u(t)$, ω is frequency, and $*$ denotes the complex conjugate. The cross-correlation in the time domain is the inverse Fourier transform of $\gamma_{ij}(\omega)$, denoted $\gamma_{ij}(\tau)$, where τ here is the cross-correlation lag-time.

It is often of practical interest (see section 3) to normalize the spectrum

of ground motion in some way such that

$$\tilde{u}(\omega) \equiv \frac{u(\omega)}{N(\omega)}, \quad (5.2)$$

where $N(\omega)$, usually a real-valued function, is the spectral normalization function. We use ' \sim ' to denote frequency normalization. In this case we end up with the spectrally normalized cross-spectrum:

$$\tilde{\gamma}_{ij}(\omega) \equiv \tilde{u}_i(\omega)\tilde{u}_j^*(\omega) = \frac{u_i(\omega)u_j^*(\omega)}{N_i(\omega)N_j(\omega)}. \quad (5.3)$$

An example is $N(\omega) = |u(\omega)|$, where $|\cdot|$ denotes the modulus. With this normalization, $\tilde{\gamma}_{ij}(\omega)$ would be the complex coherency and $\tilde{\gamma}(\tau)$ would be coherency in the time domain, the inverse Fourier transform of $\tilde{\gamma}(\omega)$.

Snieder (2004) and others have argued that under idealized conditions the time derivative of the cross-correlation will be proportional to the Green's function between the two stations where the frequency dependent proportionality constant will depend on the source spectrum of the ground motion. Aki (1957) and others have argued that these conditions may be satisfied approximately if the ensemble average of the cross-spectrum is taken,

$$\Gamma_{ij}(\omega) \equiv \langle \gamma_{ij}(\omega) \rangle, \quad (5.4)$$

where $\langle \cdot \rangle$ denotes the ensemble average. We use the upper case to represent ensemble averaging. In this case,

$$\frac{d\Gamma_{ij}(\tau)}{d\tau} \propto \begin{cases} -G_{ij}(\tau) & \tau \geq 0 \\ G_{ji}(-\tau) & \tau < 0, \end{cases} \quad (5.5)$$

where G_{ij} is the Green's function between stations i and j , G_{ji} is the reciprocal Green's function between stations j and i , and \propto denotes proportionality. This proportionality also holds for the ensemble average of the frequency normalized cross-correlation $\tilde{\Gamma}_{ij}(\tau)$.

Equation (5.5) illustrates the basis of ambient noise tomography, which is, at least in this idealized case, that the cross-correlation may be used to estimate the Green's function between a pair of stations.

We have not discussed yet the meaning of the ensemble average $\langle \cdot \rangle$. It is convenient to follow Aki (1957) and define the ensemble average as an average over time or time intervals. Let $u_i^k(t)$ and $u_j^k(t)$ be the vertical components of ground motion measured at a pair of stations i and j on a finite sequence of time intervals denoted by index $k = 1, \dots, K$. The ensemble average of the cross-correlation in the time domain, therefore, is

as follows:

$$\Gamma_{ij}(\tau) = \langle \gamma_{ij}(\tau) \rangle \approx \sum_k W_k(\tau) \gamma_{ij}^k(\tau), \quad (5.6)$$

where the functions $W_k(\tau)$ compose a set of (possibly time-dependent) time domain weights. Thus, the ensemble average can be approximated as the weighted average of the cross-correlations taken over a discrete set of time intervals. The process of ensemble averaging described by equation (5.6) is commonly referred to as “stacking”. Stacked signals are sometimes called “estimated Green’s functions” or EGFs, which is somewhat confusing because it is their time derivative that is related to the Green’s functions. We note that signals on a cross-correlation and the time derivative of the cross-correlation will have the same group velocity, which is one of the reasons for calling the cross-correlation the EGF. However, this terminology is sloppy because the phase velocities will differ.

Time τ in equation (5.6) is the cross-correlation lag-time, which can be positive or negative. It is often useful to separate the cross-correlation at positive and negative lag times as follows:

$$\Gamma_{ij}^+(\tau) = \Gamma_{ij}(\tau) \quad \text{and} \quad \Gamma_{ij}^-(\tau) = \Gamma_{ij}(-\tau), \quad \tau \geq 0. \quad (5.7)$$

A related concept is the so-called “symmetric component” of the cross-correlation, which is defined as follows:

$$\Gamma_{ij}^{sym}(\tau) = \frac{1}{2} \left(\Gamma_{ij}^+(\tau) + \Gamma_{ij}^-(\tau) \right), \quad \tau \geq 0. \quad (5.8)$$

This is simply the average of the cross-correlation reflected symmetrically about lag-time $\tau = 0$. With this definition, equation (5.5) can be rewritten as follows:

$$\frac{d\Gamma_{ij}^{sym}(\tau)}{d\tau} \propto -G_{ij}(\tau), \quad \tau \geq 0. \quad (5.9)$$

Equations similar to (5.4) - (5.9) also hold for the ensemble average of the frequency normalized cross-correlation, $\tilde{\Gamma}_{ij}(\tau)$, and its symmetric component, $\tilde{\Gamma}_{ij}^{sym}(\tau)$.

5.3 Practical Implementation: Continental Rayleigh Waves

In section 2 we noted that if certain “idealized conditions” are manifest, then the ensemble average of the cross-correlation of ambient ground motion recorded at two observing stations may be proportional to the Green’s

function between these stations. Such a function is sometimes referred to as an “estimated Green’s function”. Such idealized conditions include the azimuthal homogeneity of the ambient seismic wave field and the equipartition of energy amongst the normal modes of the medium. These conditions do not hold in the real Earth in essentially all applications. At the length scales and frequency bands of consideration in this chapter, surface waves dominate the cross-correlations; thus modal equipartition is unsatisfied. In addition, the ambient noise that propagates over long distances typically originates in the oceans and is excited at certain azimuths more strongly than others. Other strong isolated noise sources (e.g., earthquakes and certain other persistent sources) further deviate reality from ideality.

The practical challenge that faces the observational seismologist is to attempt to extract meaningful approximate or estimated Green’s functions from cross-correlations of ambient noise without the theoretical guarantee that such attempts will be successful. As mentioned in the Introduction, the aim is to minimize bias, to estimate uncertainty, and to maximize the bandwidth of observation. To do this, there are several variables referred to in section 2 that can be tuned and much of the practical work in ambient noise methodology has been dedicated to the systematic exploration of this parameter space. These variables include the tempo or the cadence rate of the cross-correlations in the time domain (T), the time domain weights ($W(t)$), and the frequency domain normalization ($N(\omega)$). A great many papers have been written by researchers who have varied these (and other) quantities in the attempt to extract reliable Green’s functions for the medium of their study. We will make no attempt to summarize these studies, but will present a general discussion of the issues involved in the choice of these variables.

Practically speaking again, the key issues that interest most researchers, especially for crustal imaging, are to expand the frequency band of observation outside the microseism band (8-20 sec), to attempt to homogenize the azimuthal content of ambient noise as much as possible, and to identify and eliminate any instrumental irregularities. In terms of optimizing azimuthal homogeneity, a major focus is the attempt to minimize the effect of earthquakes as well as persistent localized sources of noise, both of which may be azimuthally limited.

One of the key indicators of success is that precursory signals, signals that arrive prior to the signal of interest, which is typically the fundamental mode surface wave, are small in comparison to the signal of interest.

5.3.1 The Cadence Rate of Cross-Correlation

In most of the examples presented here, the length of the time series for cross-correlation, T , is one-day. After selecting one day of data, we typically first remove the instrument response, remove the mean and trend, and band-pass filter.

The choice of a one-day data length is ad-hoc and a shorter time series length is advocated by some researchers (e.g., Prieto et al., 2011). One advantage of a faster cadence rate for cross-correlation relates to the treatment of earthquake sources. With a time series length of 1-hour, for example, if an earthquake or short term instrumental irregularity is identified, the 1-hour time period can simply be discarded. One is less likely to be willing to sacrifice a whole day to eliminate such effects, so with a slower rate to cross-correlation the tendency is to introduce some sort of time-dependent weights to continuously down weight the time periods where such effects are identified, as described in the following paragraph. The downside to introducing such weights, however, is the loss of meaningful amplitude information. Thus, researchers who desire reliable amplitude information may be interested in increasing the rate of cross-correlation and applying a binary time domain weighting scheme: 0 for time periods where earthquakes or instrumental irregularities are identified and 1 for other time periods.

5.3.2 Time Domain Weighting

Most practitioners of ambient noise seismology employ a more detailed time domain weighting scheme than the binary choice mentioned in section 3.1. Some of these alternatives are designed to homogenize the ambient noise signals in azimuth by down-weighting azimuthally limited signals that are either exceptionally strong (e.g., earthquakes) or are persistent over time (e.g., 26 sec microseism, Kyushu microseism). Figure 5.3 presents three example alternatives for the time domain weights, $W(t)$: no weights, one-bit normalization, and running absolute mean weights.

The running absolute mean time-domain weighting scheme is defined as follows:

$$W(t_n) = \frac{1}{N+1} \sum_{j=n-N/2}^{n+N/2} |u(t_j)|, \quad (5.10)$$

where time is presented on a discrete grid. Thus, at time grid point t_j , the weight is the absolute mean of the seismogram in a time window of length N spanning the time point. Typically, N is chosen to be some multiple of

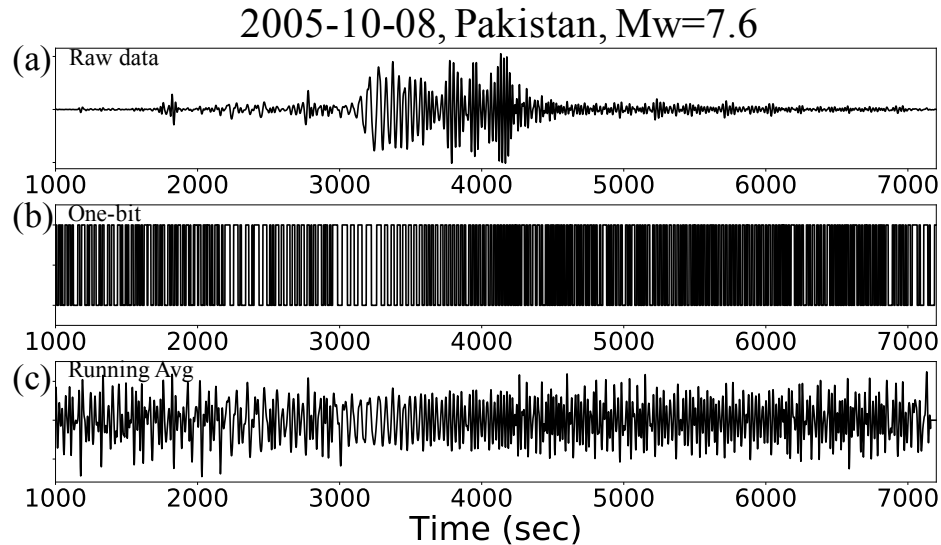


Figure 5.3 Waveforms displaying three different examples of time-domain normalization, $W(t)$, band-passed between 20 and 100 s period to clarify the contamination by the earthquake signal. Data are from station ANMO. (a) Raw seismogram showing about 6200 seconds of data around the earthquake (Mw = 7.6, Pakistan region). (b) One-bit normalized waveform in which the signal is set to ± 1 depending on the sign of the original waveform. (c) Running absolute mean normalization in which the waveform is normalized by a running average of its absolute value.

the maximum period in the band-pass filter applied to the data. To ensure that the longer periods are not filtered out, N should be chosen to be at least the length of the maximum period. Note that if $N = 0$, the approach is equivalent to one-bit normalization, in which signal amplitudes become ± 1 . One down-side of the method is that it does not surgically remove data spikes, unlike one-bit normalization, but spreads them out in time. This weighting scheme is applied before cross-correlation.

Figures 5.4a-c show the effect of applying these three weighting schemes on cross-correlations stacked over a year of ambient noise data acquired at stations ANMO and HRV. The added effect of frequency domain weighting, which is discussed in section 3.3, is shown in Figures 5.4d-f.

Figure 5.4a illustrates the motivation for applying time-domain weights. The near zero lag-time response illustrates that the recovered signals are not homogeneously distributed in azimuth, but are precursory noise, presumably from earthquakes in this case. The relative arrival time between the artifact and the real signal provides information about the azimuth of the interfering

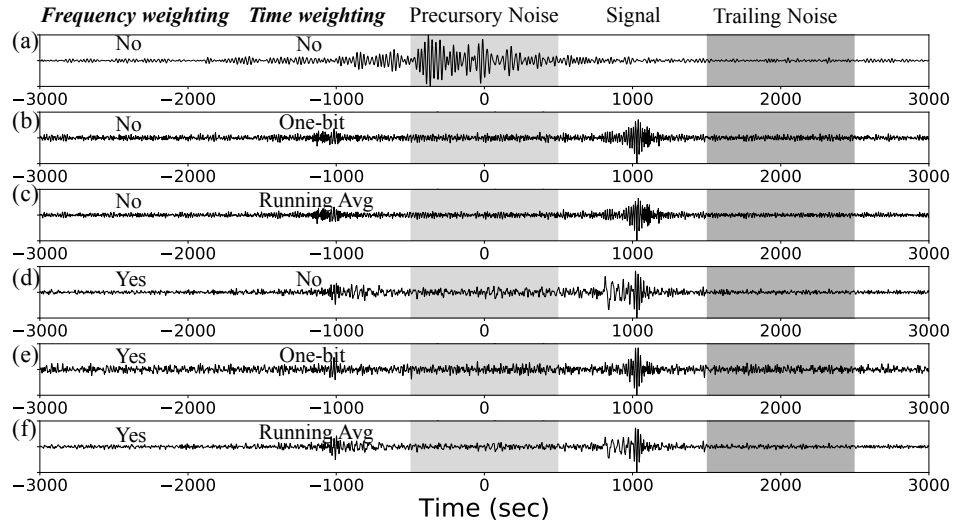


Figure 5.4 Twelve-month cross-correlation between data from the station pair ANMO-HRV (as in Fig. 5.2) for various frequency and time-domain normalizations, band-passed between 20 and 100 s period. Panels in (a)-(f) are labeled with the types of normalization applied: (a) no time or frequency domain normalization, (b) one-bit time domain normalization but no frequency domain normalization, (c) running absolute average time domain normalization but no frequency domain normalization, (d) no time domain normalization but frequency domain normalization is applied, (e) one-bit time domain normalization with frequency normalization, and (f) running absolute average time domain normalization with frequency normalization. Signal and precursory and trailing noise windows are indicated with shading. Precursory and trailing SNR for each of these cases is presented in Table 1, whose rows are ordered corresponding to (a)-(f).

source relative to the inter-station path. The near zero lag-time for the cross-correlation in Figure 5.4a reveals that the source of that signal lies predominantly in an azimuthal band nearly perpendicular to the line linking these stations.

Weighting schemes (b) one-bit normalization, and (c) running absolute average normalization, from Figure 5.3 produce correlations that reveal more realistic Rayleigh wave signals at both positive and negative correlation lags. The one-bit normalization scheme is not only simple (Fig. 5.3b, but as shown in Fig. 5.4b) it is remarkably effective. Table 1 presents signal-to-noise ratios (SNR) computed in two period bands for the recordings in Figure 5.4a-c. Signal is the maximum amplitude in the time domain in the signal window (identified in Fig. 5.4b on the positive lag in this case), which is filtered into the bands between 10-20 s and 20-100 s period in the table. Noise is the root

mean square (RMS) in the time domain measured either in the precursory or trailing window. In the absence of frequency weights, the signal to noise ratio is largest for the running absolute mean normalization, but the one-bit normalization method also performs well.

As discussed in section 4, in extracting Love waves we seek to apply the same time domain normalization to both horizontal components. The one-bit filter is so intimately related to each component that defining a single filter to apply to both components is impractical. In addition, as we discuss below the one-bit normalization methods tends not to perform well with spectral weighting designed to increase the band-width of the cross-correlations. For these reasons we tend to prefer the running absolute mean weighting scheme (c) of Figure 5.3, irrespective of the simplicity of one-bit normalization. Results shown in the remainder of this chapter are based on running absolute mean time-domain weighting scheme unless explicitly noted otherwise.

5.3.3 Frequency Domain Weighting

Frequency domain weighting is applied for two main reasons: to broaden the bandwidth of the estimated Green’s functions and to diminish the effect of band-limited spatially localized sources such as the 26 s microseism (e.g., Shapiro et al., 2006) or the Kyushu microseism (e.g., Zeng and Ni, 2010). Like time domain normalization, it is applied to seismic records prior to the cross-correlation. The effect on cross-correlations of applying frequency domain normalization is exemplified in Figures 5.4d-f.

Ambient noise is not spectrally white; that is, its spectrum is not flat. Rather, in the frequency band of regional to global scale tomography (e.g.,

Table 5.1 SNR using precursory (pre) and trailing (trail) noise for Figure 5.4 for different time and frequency domain weighting schemes in two period bands. RA stands for the running average.

Normalization		10–20 sec		20–100 sec	
Freq	Time	A_{max}/RMS_{pre}	A_{max}/RMS_{trail}	A_{max}/RMS_{pre}	A_{max}/RMS_{trail}
No	No	1.478	6.291	0.650	8.074
No	one-bit	12.273	14.928	8.189	10.586
No	RA	14.104	17.993	9.481	12.169
Yes	No	13.446	18.916	8.588	22.982
Yes	one-bit	10.555	10.854	6.323	7.319
Yes	RA	16.626	20.217	9.274	14.032

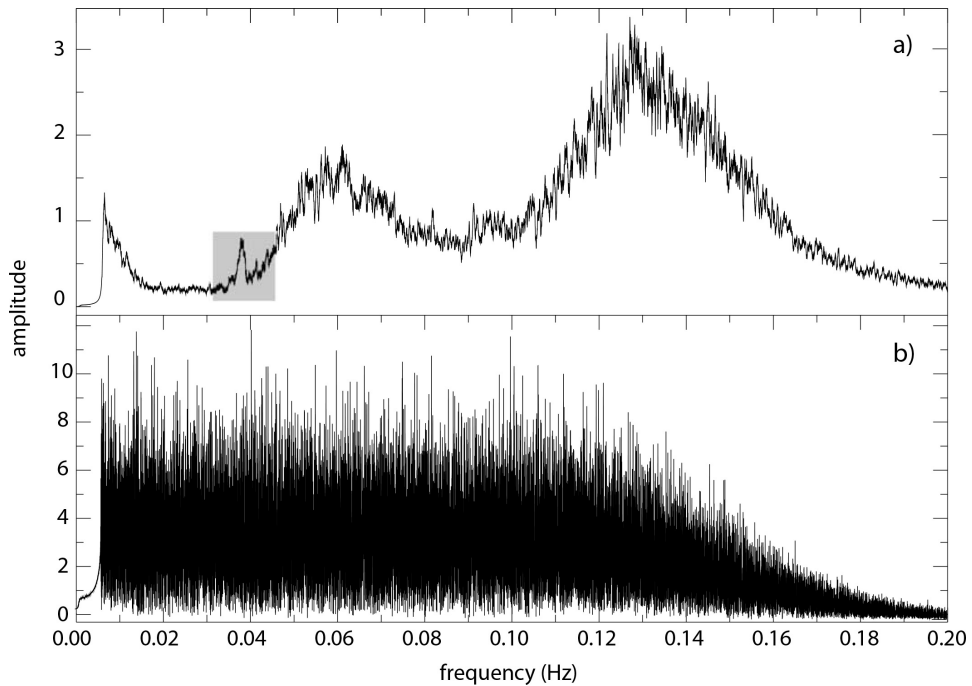


Figure 5.5 (a) Raw and (b) spectrally normalized amplitude spectra for station HRV from July 5, 2004. The shaded box in (a) shows the 26 s Gulf of Guinea microseism. The tapering at the ends reflects the 7-150 s period bandpass filter. This figure is taken from Fig. 7 of Bensen et al. (2007).

5 - 200 s period), it is peaked near the primary (~ 15 s period) and secondary (~ 7.5 s period) microseisms and then rises again at periods above 50 s to form Earth “hum” (see Chapter 1 (McNamara and Boaz, 2018)). Figure 5.5a shows an example spectrum for one summer day of vertical component data from station HRV, which illustrates the two microseismic humps and the rise of the noise level at low frequencies. In addition, isolated peaks are also sometimes apparent in ambient noise, as the grey shaded box in Figure 5.5a illustrates around the 26 s microseism. Because the 26 s microseism propagates coherently over long distances, it appears even more strongly on cross-correlations between distant stations, as illustrated by Figures 5.6ab. Similarly, the dual-band nature of the microseismic component of ambient noise is also accentuated by cross-correlation as Figures 5.7ac illustrates.

One means of frequency domain weighting is spectral whitening, which flattens the observed spectrum in some way. Whitening acts to broaden the band width of ambient noise and also reduces the impact of spatially isolated persistent noise sources. Whitening can take several forms. Some

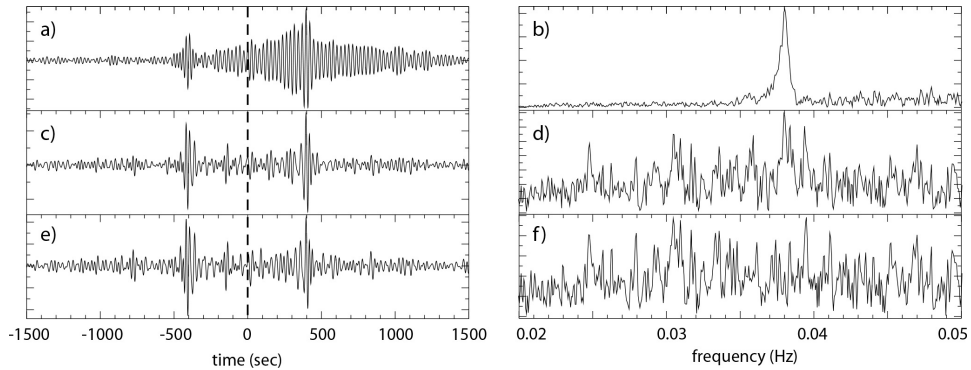


Figure 5.6 Illustration of the effect of the 26 s microseism on cross-correlations of ambient noise and its removal by spectral whitening. (a) Cross-correlation between 12 months of data from stations ANMO and CCM (Cathedral Cave, MO, USA). The broad monochromatic cigar-shaped arrival is the effect of the 26 s microseism. (b) Amplitude spectrum of the cross-correlation in (a) showing the peak near 26 s period. (c-d) Similar to (a) and (b), but for data that were spatially whitened prior to cross-correlation, such that the effect of the 26 s microseism has been largely eliminated. (e-f) Similar to (c) and (d), but the data were notch-filtered around 26 s period prior to cross-correlation. The notch filter delivers little improvement in eliminating the 26 s microseism signal at the expense of losing dispersion information in the period band of the notch filter. This figure is taken from Fig. 8 of Bensen et al. (2007).

researchers advocate for dividing the observed spectrum by its modulus in some finite band, so that $N(\omega) = |u(\omega)|$ in that band. This results in an absolutely flat spectrum and the construction of the coherence after cross-correlation, as discussed in section 2. One of several other alternatives is to normalize by a smoothed version of the amplitude spectrum. In this case, $N(\omega) = S(\omega) \star |u(\omega)|$, where $S(\omega)$ is the smoothing filter and \star represents convolution. An example showing the effect of this operation is presented in Figure 5.5b. Example results of such spectral smoothing on cross-correlations are presented in Figures 5.4, 5.5, and 5.7. A whitened spectrum typically does not remain white after cross-correlation, presumably because the geographical distribution of microseismic sources is more favorable to recovering some signals than others. However, as illustrated in Figures 5.7bd the result is broader band and more continuous than without spectral whitening (Fig. 5.7ac), and is particularly effective at improving the quality of signals at frequencies lower than the microseismic band. Whitening is particularly successful at eliminating the effect of the 26 sec microseism as Figures 5.6c-f

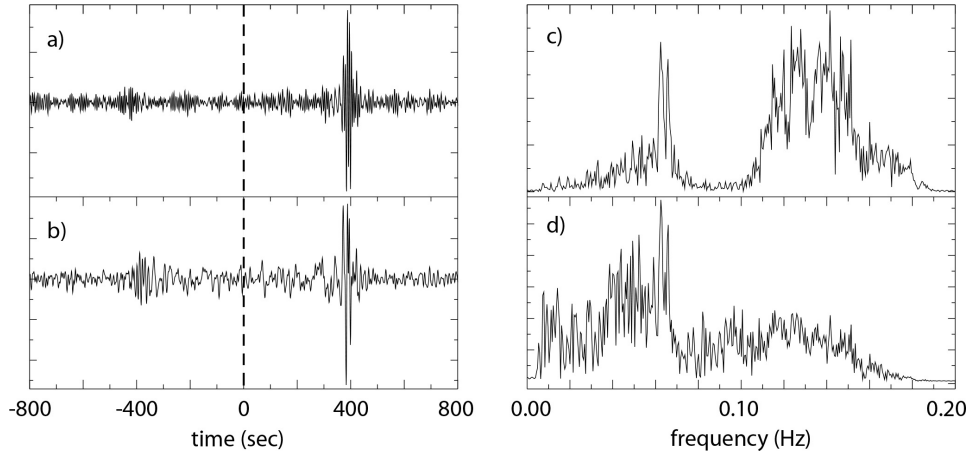


Figure 5.7 Comparison of cross-correlations and their amplitude spectra without (a, c) and with (b,d) spectral whitening, computed for one month of data (April, 2004) using stations CCM and SSPA (Standing Stone, PA, USA). Primary and secondary microseisms are more dominant without spectral whitening (c) and low frequencies are accentuated with spectral whitening (d). This figure is taken from Fig. 9 of Bensen et al. (2007).

shows. The application of a notch filter around the 26 s microseism provides little improvement over spectral whitening without the notch.

Spectral whitening appears to be less successful at removing some local persistent noise sources, such as the Kyushu signal generated from Aso volcano, from cross-correlations between stations in China or locally isolated wave-wave interactions. Zheng et al. (2011) found that they needed to use the opposite correlation time lag from the direction to Aso volcano. Tian and Ritzwoller (2017) identified persistent signals in their cross-correlations between OBS stations that they argued were related to local persistent microseismic sources in shallow waters of the Juan de Fuca plate.

Figures 5.4d-f illustrate how the application of frequency weights brings out the longer periods, which arrive earlier than the shorter periods in the Rayleigh wave train. Table 1 quantifies this effect. Two things are noteworthy. First, one-bit normalization does not work well in conjunction with frequency domain weights, and cross-correlations tend to be more band limited than when running absolute mean normalization is applied. Second, the highest SNR at long periods actually results without time domain weighting, which is an indication that the length of the time window we used to measure the absolute mean (N in eqn. 5.10) was probably too short to optimize results at the longer periods.

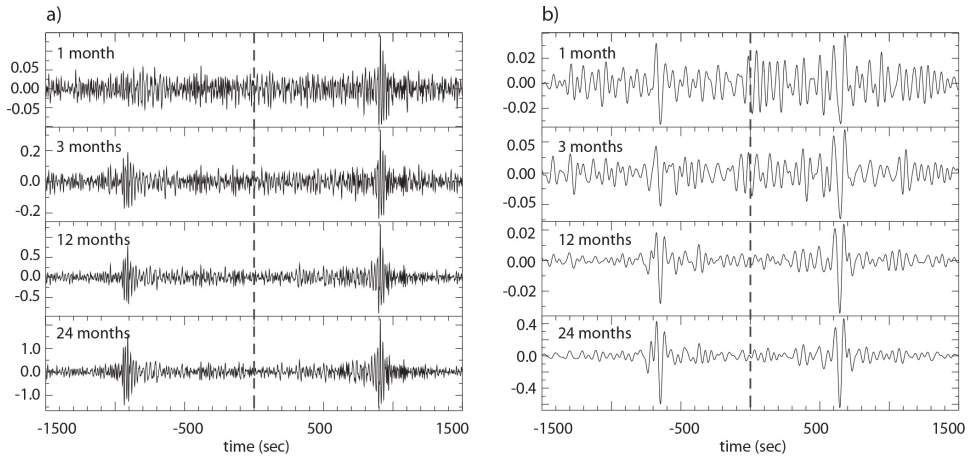


Figure 5.8 Example cross-correlation results with different total time series lengths (labeled on each panel) and in different pass bands: (a) 5 - 40 s period and (b) 40 - 100 s period. Both positive and negative correlation lags are shown. Data are from the station pair ANMO and DWPF (Disney Wilderness Preserve, FL, USA). This figure is adapted from Fig. 10 of Bensen et al. (2007).

Results shown here use smoothed spectral whitening unless explicitly indicated otherwise. Shen et al. (2012) present a revised method of spectral normalization in which spectral whitening is performed on shorter time windows along with time-domain normalization that they argue further extends the spectral band of observation to longer periods.

5.3.4 Cross-Correlation and Stacking

After the data have been prepared for each day (or for a shorter or longer duration T), including spectral and temporal normalization if desired, we cross-correlate and stack over time as shown in equation (5.6). Example results for different total time series lengths are shown in Figure 5.8. The SNR typically grows with stacking length. We define the SNR as the peak amplitude in the signal window divided by the RMS amplitude in the noise window, as illustrated in Figure 5.4. Typically, signal to trailing noise grows approximately as the square root of the time series length. This is because signal amplitude tends to grow approximately linearly with time and trailing noise grows approximately as the square root of time as shown by Lin et al. (2011). There can be deviations from the square root of time rule that depend on time variations in the strength of ambient noise, but it is a useful rule-of-thumb. Bensen et al. (2007) reported a deviation from the square

root of time rule, but much of this was related to how they measured time series length.

The SNR as we define it in the previous paragraph is a useful indicator of data quality and is used regularly as an automated data selection metric, as discussed in section 6. However, because precursory noise is indicative of incomplete destructive inference for off-inter-station axis events, the ratio of peak signal to the RMS of precursory noise level may be a better metric to indicate the extent of convergence of the algorithm.

5.3.5 Measurement of Surface Wave Dispersion

After the daily cross-correlations have been computed and stacked, group and phase speeds can be measured as functions of the period on the resulting waveform, $s(t)$, using a variety of different time domain and frequency domain methods. Here we describe a time domain method, which is traditional frequency-time analysis (e.g., Levshin and Ritzwoller, 2001). Other researchers prefer frequency domain methods (e.g., Ekström et al., 2009).

Roughly following the terminology and notation of Bracewell (1978), the Fourier transform of $s(t)$ is defined with a positive exponent as:

$$S(\omega) = \int_{-\infty}^{\infty} s(t) \exp(i\omega t) dt. \quad (5.11)$$

We obtain group and phase time measurements by considering the “analytic signal”, which is defined in the frequency domain as

$$S_a(\omega) = S(\omega) (1 + \text{sgn}(\omega)), \quad (5.12)$$

where “sgn” is the sign function. The inverse Fourier transform of equation (5.12) in the time domain is the analytic time series

$$s_a(t) = s(t) + ih(t) = A(t) \exp(i\phi(t)), \quad (5.13)$$

where $h(t)$ is the Hilbert transform of $s(t)$ and the positive sign in front of the $h(t)$ is chosen to be consistent with the positive exponent in the Fourier transform, equation (5.11). The frequency-time function is constructed by applying to the analytic time series a set of narrow bandpass Gaussian filters with center frequencies ω_0 :

$$S_a(\omega, \omega_0) = S(\omega) (1 + \text{sgn}(\omega)) G(\omega - \omega_0), \quad (5.14)$$

where

$$G(\omega - \omega_0) = \exp\left(-\alpha \left(\frac{\omega - \omega_0}{\omega_0}\right)^2\right), \quad (5.15)$$

where α is a tunable parameter that defines the complementary resolutions in the time and frequency domains and is commonly made range dependent (e.g., Levshin et al., 1989).

Inverse Fourier Transforming each band-passed function $S_a(\omega, \omega_0)$ back to the time domain yields the 2D envelope function, $A(t, \omega_0)$, and phase function, $\phi(t, \omega_0)$. Group speed is measured from $A(t, \omega_0)$ and phase speed from $\phi(t, \omega_0)$. $A(t, \omega_0)$ is sometimes called the “frequency-time analysis” or “FTAN” diagram, an example of which is shown later in the chapter. The group travel time, t_g , is measured using the peak of the envelope function at each center frequency such that group velocity $U(\omega) = r/t_g$, where r is the inter-station distance. If the group speed changes rapidly with center frequency, Bracewell suggests that the center frequency be replaced by the so-called “instantaneous frequency”, ω , at t_g : $\omega = [\partial\phi(t, \omega_0)/\partial t]_{t=t_g}$.

For instantaneous frequency ω , the phase of the cross-correlation function observed at time t can be expressed as follows:

$$\phi(t, \omega) = kr - \omega t + \frac{\pi}{2} - \frac{\pi}{4} + n \cdot 2\pi, \quad (5.16)$$

where n is an integer. The negative sign in front of the ωt is chosen to be consistent with choice of the positive exponent in the Fourier transform, equation (5.11). With this definition, phase decreases with an increase in time. In equation (5.16), k is the wavenumber, $\pi/2$ is the phase shift from the negative time derivative relating the stacked cross-correlation with the Green’s function (eqn. (5.5)), $-\pi/4$ is the asymptotic remnant of the Bessel function under the far-field approximation (Snieder, 2004), and $n \cdot 2\pi$ is the intrinsic phase ambiguity of phase measurements. The $\pi/2$ phase shift can equivalently be thought of as accounting for the phase shift between the applied force and the displacement response of the system.

From equation (5.16), the phase velocity c at instantaneous frequency ω when measured on the cross-correlation function is given by

$$c = \frac{\omega}{k} = \frac{r\omega}{\phi(\omega, t_g) + \omega t_g - \pi/4 - n \cdot 2\pi} \quad (5.17)$$

and the phase time is r/c and n is an unknown. n is determined, essentially, by using reference dispersion curves and iterating. Its determination is discussed at length by Lin et al. (2008). We only note that n is more easily resolved at longer periods and once it is known for a station-pair at any frequency it is known for all frequencies.

Figure 5.9 presents a few examples of Rayleigh wave phase and group speed dispersion curves measured between a station in New Mexico and a set

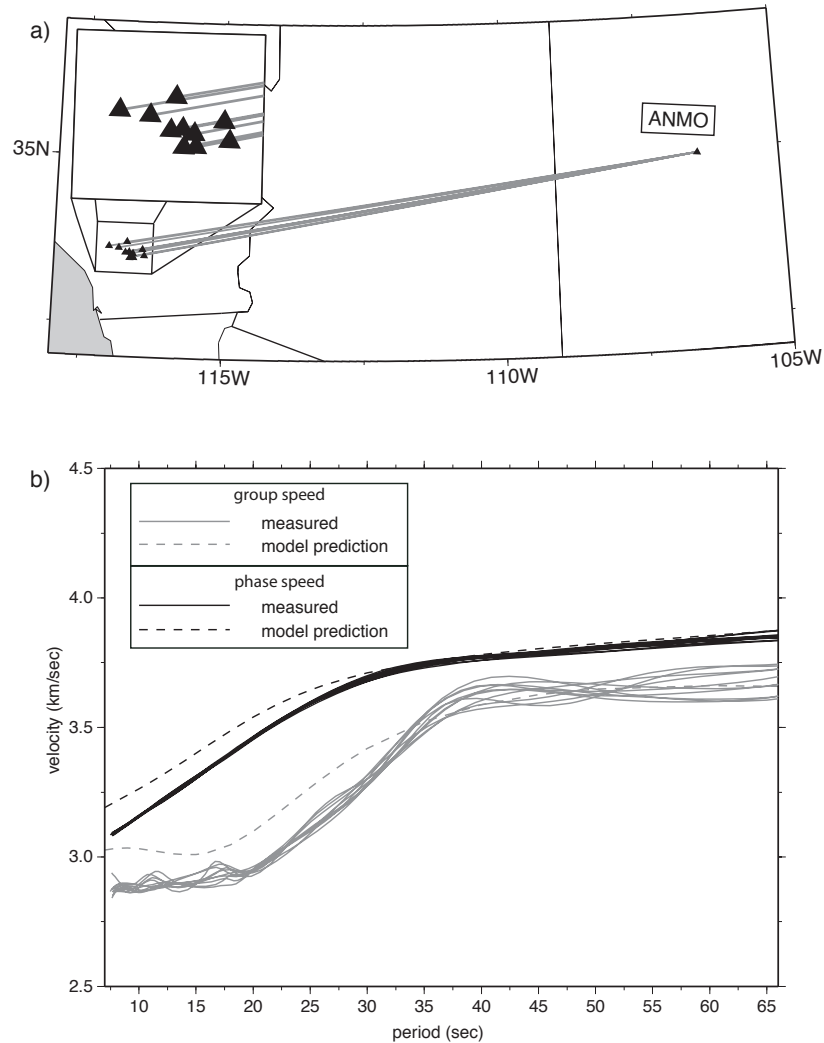


Figure 5.9 Group and phase speed measurements obtained from year-long correlations between station ANMO and 10 stations in southern California. (a) The cluster of 10 paths. (b) Measurements are shown with solid lines and the prediction from the global 3D model of Shapiro and Ritzwoller (2002) is shown with the dashed lines. This figure is modified from Fig. 16 of Bensen et al. (2007).

of closely located stations in Southern California. It illustrates an important point. Phase speed is typically determined more reliably than group speed.

Researchers often apply an inter-station distance criterion such that dispersion measurements are discarded unless the inter-station spacing is greater

than two or perhaps more wavelengths. One reason for this is that time domain dispersion measurements reflected in equations (5.16) and (5.17) are based on a far-field approximation, and the far-field is typically defined as setting on after two or more wavelengths. For this reason, frequency domain dispersion measurements may be preferable (e.g., Ekström et al., 2009) for short inter-station distances. Luo et al. (2015) present evidence, however, that time domain methods are reliable at least down to an inter-station spacing of one wavelength. A more compelling reason to apply a multiple wavelength selection criterion is that at longer inter-station distances, signals of interest become more separated from precursory noise and the interference from precursory noise lessens appreciably. This is true for both the time or frequency domain measurements of phase speed.

5.3.6 Closing Remarks

The methods presented here are devised to recover meaningful and reliable surface wave dispersion information. Optimal methods probably depend on the nature, time period, and location of the experiment, and the reader is encouraged to be creative and try their own ideas. It should be remembered, however, that both the time-domain normalization and frequency whitening methods presented here, and presumably most others, are non-linear. This means that the order of application of the time-domain and frequency domain filters matters.

5.4 Practical Implementation: Continental Love Waves

In early research, ambient noise tomography was applied predominantly to vertical component seismic records to recover fundamental mode Rayleigh waves. This was partially because the generation of Love waves in ambient noise was (and remains) more poorly understood than the generation of Rayleigh waves (see Chapter 3 (Ardhuin et al., 2018)). Thus, it was not clear initially if ambient noise cross-correlations would recover Love waves, and less attention was paid to horizontal components. Nevertheless, it is now understood that Love waves are well represented in ambient noise and they provide important information about both crustal and uppermost mantle anisotropy through a growing number of studies (e.g., Moschetti et al., 2010; Lin et al., 2011; Xie et al., 2013, 2017).

There are three principal differences in processing ambient noise data for Love waves compared to Rayleigh waves. (1) First, to retain meaningful geo-

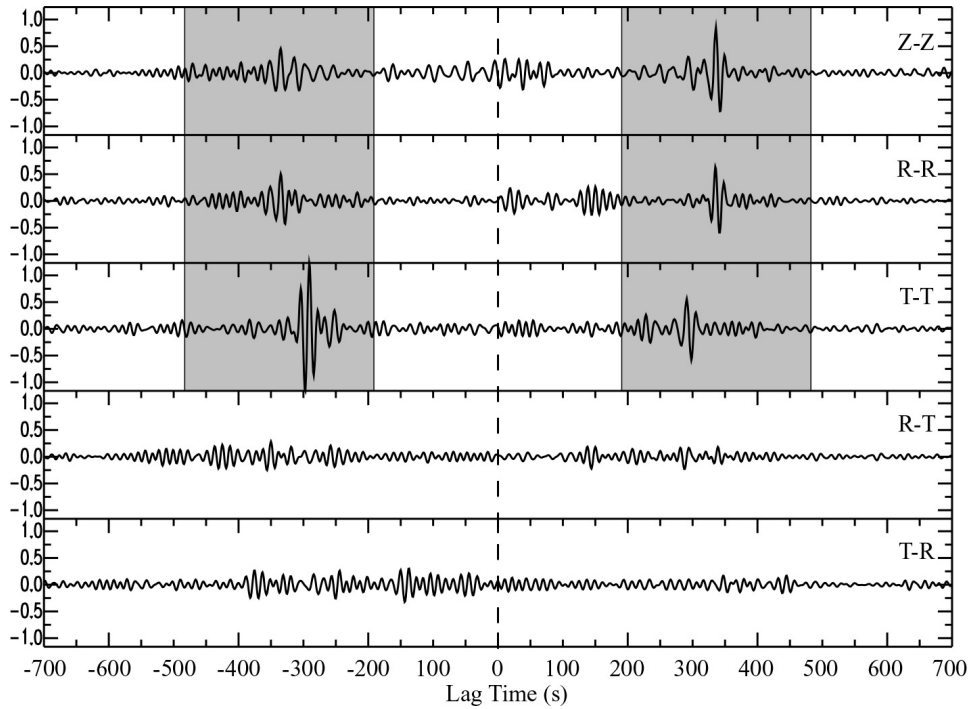


Figure 5.10 Normalized cross-correlations observed between two USArray stations, 116A (Elroy, Arizona) and R06C (Coleville, CA). The grey boxes indicate a group speed window between 2 km/s and 5 km/s. Vertical, radial, and transverse are indicated with Z, R, and T, respectively. Results are band-pass filtered between 10 and 25 s period. This figure is taken from Fig. 3 of Lin et al. (2008).

metrical information upon rotation transverse to the inter-station direction, the East and North component records for each station must be normalized identically (in both time and frequency) prior to cross-correlation. This can be done in a variety of ways, but Lin et al. (2008) suggest normalizing by the maximum of the values from the two components (time domain weight, frequency domain amplitude at each frequency). (2) Second, cross-correlations are computed between all components. Given the three-components of the seismograms at two stations (Z - vertical, E - East, N - North), nine cross-correlations can be performed: ZZ, EE, NN, EN, NE, ZN, NZ, ZE, EZ, where the first letter represents the component of the first station and the second letter the component of the second station. (3) Finally, the cross-correlations are rotated into the Radial (R) and Transverse (T) components, each of which point in the same direction at both stations. Rotating after cross-correlation is computationally more efficient than rotating

before cross-correlation. The resulting four horizontal cross-correlations are TT, RR, TR, and RT, which are computed by rotating the four components EE, EN, NN, and NE.

An example of cross-correlations for several rotated components is presented in Figure 5.10. Rayleigh waves are observed at both positive and negative lags on the ZZ and RR components. Love waves, which are faster than Rayleigh waves in this period band, appear on the TT component. If Love and Rayleigh waves are confined predominantly to the T and R components, respectively, the RT and TR components will not show coherent arrivals, as exemplified here. The relative amplitudes for Rayleigh and Love waves on the two correlation lags differ, such that Rayleigh waves are stronger on the positive lag and Love waves on the negative lag, which means that the azimuthal content of Rayleigh and Love waves differ. Contrary to initial expectations, Love wave amplitudes on the TT components are often higher than Rayleigh wave amplitudes on either the ZZ or RR components. Love waves tend to be narrower band than Rayleigh waves, however, and Love wave dispersion measurements commonly do not extend to as long of periods as Rayleigh waves. This may reflect a narrower bandwidth of excitation for Love waves, but the bandwidth of Love wave dispersion measurements on TT components is similar to Rayleigh waves on RR components; thus the relative lack of longer period Love wave dispersion measurements probably results mostly from the higher noise levels on horizontal components.

5.5 Practical Implementation: Ocean Bottom Rayleigh Waves

The primary assumption that underlies ambient noise tomography is that seismic waves generated by noise sources propagate coherently between the pairs of stations from which recordings are cross-correlated. Highly localized seismic waves that are generated near one station but do not propagate to the second station will corrupt ambient noise cross-correlations and compromise the effectiveness of ambient noise tomography. Such local noise sources are particularly strong in ocean bottom environments and are reflected in higher ambient noise levels, particularly on horizontal components of ocean bottom seismometers (OBS). The data processing procedures discussed in sections 3 and 4 have been developed for application to land-based stations and are not calibrated for ocean-bottom environments. Nevertheless, several researchers have used data processing schemes similar to these to produce the first studies of ambient noise tomography using OBSs to image crustal and mantle

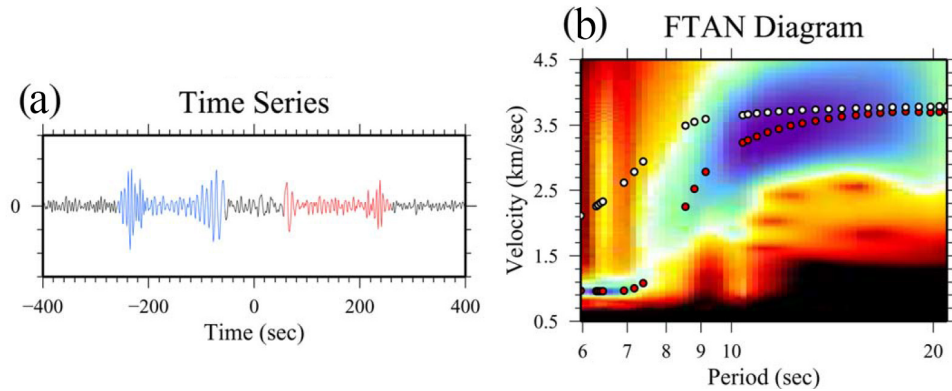


Figure 5.11 (a) Example 6-month vertical component cross-correlation for deep-water stations J29A and J47A near the Juan de Fuca Ridge recorded as part of the Cascadia Initiative. (b) Frequency-time analysis (FTAN) diagram showing Rayleigh wave dispersion from the symmetric component in (a): red dots are group speed and white dots are phase speed. The background color is the envelope amplitude, $A(t, \omega)$, discussed in section 3.5. This figure is adapted from Fig. 1 of Tian et al. (2013).

structures (e.g., Harmon et al., 2007; Gao and Shen, 2015; Tian et al., 2013; Yao et al., 2011) and to determine the directional dependence of ambient noise (e.g., Tian and Ritzwoller, 2015).

An example cross-correlation and associated FTAN diagram are presented in Figure 5.11 for two deep water stations near the Juan de Fuca Ridge. Useful cross-correlations based on OBS data using the land-based data processing procedures described above result only between the relatively quiet deep water stations or between deep water and land stations. Such recordings are typically narrow band, extending from less than about 5 s period up to about 20 s, although longer periods can be recovered if one of the stations is on land. Love waves are much more difficult to recover. Local noise levels are high at stations in all but the deepest water, for example near the Juan de Fuca Ridge in the Cascadia Initiative experiment, and make even the vertical components of these stations difficult to use in ambient noise tomography.

As seen in Figure 5.11, Rayleigh waves observed on OBSs recovered from ambient noise bifurcate into slow ocean propagating waves (< 8 s period) and fast solid earth propagating waves (> 10 s period). It is the latter that provide information about the solid earth. We would like data processing methods targeting ocean bottom environments to help extend the observations to longer periods in order to improve constraints on mantle structures. We

would also like to make observations in shallower water more useful for ambient noise tomography.

The nature of local noise on ocean bottom seismic recordings has been well studied (e.g., Webb, 1988; Duennebier and Sutton, 1995), and two types of noise are considered most important in degrading local conditions: tilt noise and compliance noise. Tilt noise is produced by seafloor currents rocking unstably situated seismometers, and is most significant where bottom currents are strongest. Compliance noise is produced by pressure variations induced by ocean gravity waves that deform the solid earth below the seismometer, and is most significant where the ocean is shallow enough for waves on the ocean's surface to couple to the solid earth. Tilt and compliance noise are local sources of noise, which are distinct from the coherently propagating long range noise that is the basis for ambient noise tomography. Both types of local noise are strongest in shallow water, although the depth extent of compliance noise is frequency dependent. Pressure variations induced by surface gravity waves decay with depth faster at higher frequencies, thus for a given water depth there is a cut-off frequency above which compliance noise is less important. Compliance noise can extend to quite deep waters, but only at very long periods.

Crawford and Webb (2000) and Webb and Crawford (1999) showed that both types of local noise are greatly reduced by predicting the effect of tilt and compliance on vertical components based on the horizontal components and a local pressure gauge, respectively. In their methods, time dependent transfer functions are found that convert horizontal noise and local pressure to the vertical component record, and then these predictions are subtracted from the vertical component. These so called “denoising” techniques have been shown to improve the SNR of earthquake data recorded on the seafloor and to reduce distortions (e.g., Ball et al., 2014; Bell et al., 2015; Dolenc et al., 2007). Additionally, Bowden et al. (2016) and Tian and Ritzwoller (2017) have shown that these methods also improve vertical (ZZ) component cross-correlations of ambient noise by improving the SNR of the first-overtone and the fundamental mode Rayleigh waves, particularly for shallower water stations, and, importantly, by extending the measurements to longer periods. Tian and Ritzwoller (2017) also showed that the methods produce records that provide more information about the origin of the coherently propagating ambient noise that is the basis for ambient noise tomography.

Figure 5.12 presents example record sections of vertical component ambient noise cross-correlations in two pass-bands observed using Cascadia Initiative data from the Juan de Fuca Plate. The common station in the

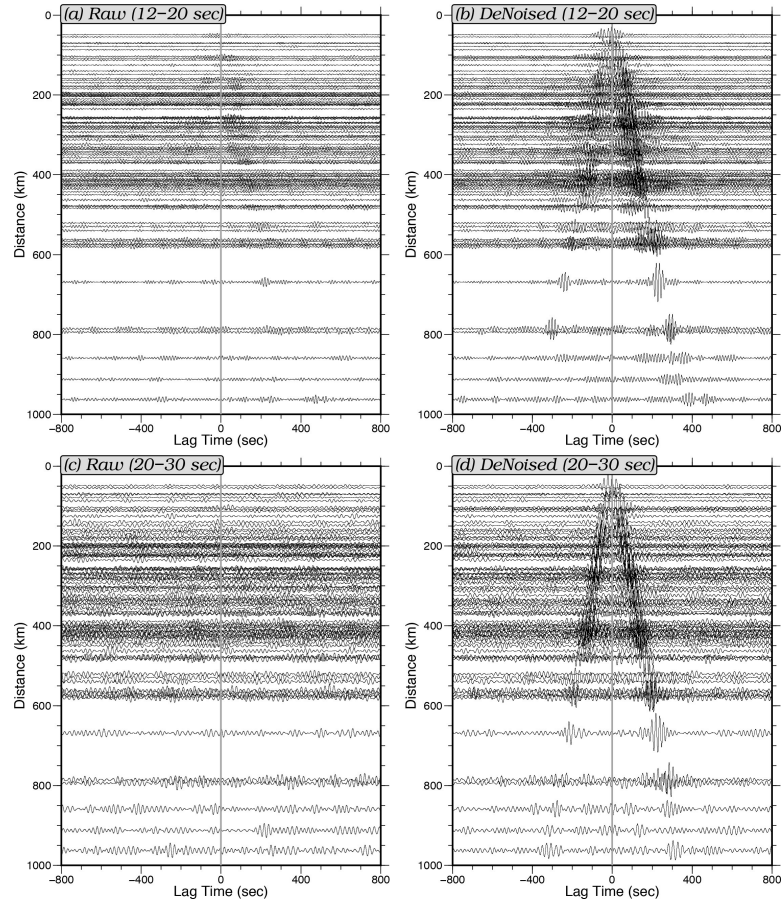


Figure 5.12 Record section of vertical component ambient noise cross-correlations for shallow water station J49A (123 m water depth) from the Cascadia Initiative on the Juan de Fuca plate, in which between 160 and 270 daily cross-correlations are stacked. (a,c) So-called “Raw” cross-correlations are shown in which only land-based data processing has been applied, including temporal normalization and spectral whitening. (b,d) “De-Noise” cross-correlations in which each record has had tilt and compliance noise removed prior to application of the same temporal normalization and spectral whitening procedures applied in the raw cross-correlations. Two period bands are shown: (top row) 12-20 s period, (bottom row) 20-30 s period. In both bands Rayleigh waves emerge more clearly with the local noise sources, tilt and compliance, removed. This figure is adapted from Fig. 8 of Tian and Ritzwoller (2017).

record section is in shallow water, station J49A at a depth of 123 m. The reduction of tilt and compliance noise greatly improves the SNR of the re-

covered Rayleigh waves, particularly at periods above 20 s that are difficult to observe without de-noising. Improvements extend up to about 40 s period.

These de-noising steps do not reduce the effect of local noise on the horizontal components, and therefore do not improve the ability to observe Love waves in ocean bottom settings. This remains a technical challenge for the future.

5.6 Reliability

As discussed earlier, there is no theoretical guarantee that the computed cross-correlations obtained using the data processing methods we describe here or others will reliably reproduce Green's functions (see also Chapter 4 (Fichtner and Tsai, 2018)). The inhomogeneous distribution of ambient noise caused by temporally persistent and spatially localized sources (e.g., 26 s Gulf of Guinea microseism, Kyushu microseism), by strong temporally and spatially localized sources (e.g., earthquakes), by highly localized incoherently propagating noise sources near one station, by a short duration of observation, and so forth, can vitiate the cross-correlation and limit its utility. Given the fact that such circumstances do arise in practice, we now consider three questions, the first two of which are:

Question 1. What tools can the observer bring to bear to determine whether a given cross-correlation is meaningfully related to the Green's function between the pair of stations from which it is computed?

Question 2. How can the observer quantify the extent of this fidelity, if it is deduced that the cross-correlation does provide a reasonable approximation to the Green's function?

To address these questions, we find it useful to think about the conditions that necessarily relate observed cross-correlations with Green's functions. The first of these questions is discussed in section 6.1. The second, which is related to the estimation of uncertainties, is discussed in section 6.2.

There is a third and final question:

Question 3. How do we know if the results are right?

This is different than asking if a measurement is acceptable. As we will see, acceptability depends to a substantial degree on quantifying the variability of the observations such that acceptable measurements exhibit low variability. There are, however, systematic errors that can bias results without introducing variability. Question 3, therefore, relates to an assessment of the nature and extent of systematic errors, which is discussed in section 6.3.

We base this analysis in terms of conditions that are sufficient to establish the correspondence of a cross-correlation with the Green's function.

5.6.1 Acceptance or Rejection of a Cross-Correlation

We define a necessary condition X as follows.

Necessary Condition: If an ensemble-averaged (temporally-stacked) cross-correlation $\Gamma_{ij}(t)$ computed from recordings observed at stations i and j is a good approximation to the Green's function $G_{ij}(t)$ between the stations, consistent with equation (5.5), then criterion X will be satisfied.

Necessary conditions are desired characteristics that would be satisfied if a cross-correlation in fact is a reasonable approximation to the Green's function. Together they define a set of criteria to test the hypothesis that a given cross-correlation acceptably approximates a Green's function and therefore is worthy of acceptance in an experiment. If a necessary condition X is not satisfied for a given cross-correlation, then there is reason to consider rejecting the cross-correlation from further consideration. This data acceptance and rejection stage is a critical part of the data processing at the heart of ambient noise tomography.

It is up to the observer to define the necessary conditions that form the basis for the acceptance or rejection of cross-correlations in a given experiment. We list several criteria that have played useful roles as necessary conditions in a number of studies. These criteria, a subset of them, or in conjunction with others can be thought of as a set of filters applied to cross-correlations of ambient noise before they are welcome as a final component of an experiment.

(1) **Geological coherence.** Surface waves are sensitive to relatively shallow earth structures about which other information often exists. We, therefore, expect qualitative similarity of dispersion measurements obtained from ambient noise cross-correlations with geological structures. If measurements disagree with considered judgments about the structure of the Earth, it is either a very interesting observation or a cause for concern about the measurement. For example, at periods below about 15 s group and phase speeds tend to be depressed in well understood ways by sedimentary basins. An observation of high group or phase speeds at short periods in sedimentary basins is either an error or high speed material (perhaps of volcanic origin) must reside near the surface of the basin, as it does in the Pasco Basin in southern Washington.

(2) High SNR. As discussed above, the ratio of peak signal amplitude to the RMS of trailing noise tends to increase as the square root of observing time, as illustrated in Figure 5.8. If this proves not to be the case, then the reason should be resolved by the observer. SNR affects the variance in group and phase speed measurements. SNR values of 10-20 are commonly used acceptance criteria, but in data starved circumstances, a SNR as low as 5-8 has been used in some circumstances.

(3) Stability. This condition relates to how cross-correlations or measurements made on them are modified when subjected to small changes in observing conditions, such as station location or time period of observation (seasonal variability, for example). Figure 5.9 presents an example of how group and phase speed vary as a function of observing station. Observations of the variability of surface wave dispersion measurements are often used as conservative estimates of the uncertainty of the measurement.

(4) Reduction in precursory noise. As the total time series length of the stacked cross-correlations increases, it is expected that the relative amplitude of the arrivals precursory to the signal of interest will decrease. In this case, longer observing times will yield better surface wave dispersion measurements. The rate of increase of the signal to precursory noise will depend on local observing conditions, but if signal level does not increase with increasing time series length relative to precursory noise, the observer should be concerned. It may be the case that the precursory noise appears only on a particular lag related to the azimuth of a spatially localized noise source, as with the Kyushu microseism in the study by Zheng et al. (2011). In this case, a cross-correlation may be salvaged by using only the correlation lag opposite from where the noise source arrives. This illustrates that it is a good idea for the observer to subject both lags of the cross-correlation independently to the selection criteria listed here, and decide which inter-station cross-correlations and lags to accept or reject based on this full set of information.

(5) Self-consistency. We refer here to two characteristics of cross-correlations as “self-consistent”. First, group and phase speed measurements form period-dependent dispersion curves, which for realistic earth structures typically vary smoothly with period. Dispersion measurements that perturb the smoothness of the dispersion curve are suspect. Second, if both the positive and negative lags of a cross-correlation pass other selection criteria and are believed to be of high quality, then they should provide similar group and phase speed measurements. There are limitations to this criterion, as one lag may be enriched at different frequencies than the other. However, this criterion has been used by Stehly et al. (2007) and Lin et al. (2007) to discover station

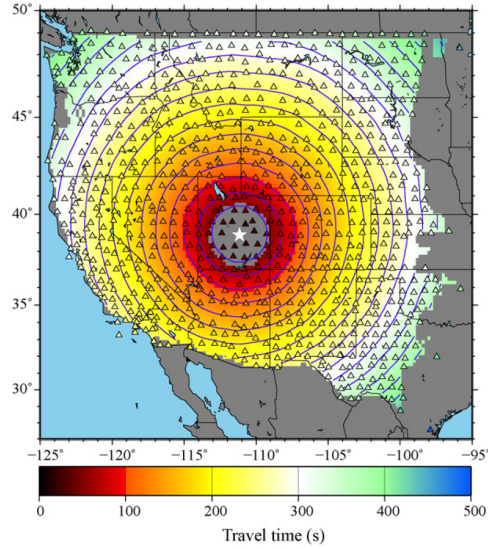


Figure 5.13 The 24 s Rayleigh wave phase travel time surface computed from cross-correlations of ambient noise observed across the western US based on central station (USArray, Transportable Array) Q16A in Utah. Travel time lines are presented in increments of wave period. The map is truncated within two wavelengths of the central station and where the travel times are not well determined. Station Q16A operated simultaneously with the 843 stations shown (triangles), but only for a short time near the western and eastern boundaries of the map. This figure is taken from Fig. 2 of Ritzwoller et al. (2011).

timing errors and differences between dispersion measurements at positive and negative lags may also provide useful information about measurement uncertainties.

(6) Cross-consistency and simplicity. The determination of cross-consistency, the agreement of a cross-correlation between one pair of stations with those between other pairs, is less straightforward to test than self-consistency. We usually do this with the group and phase speeds (or times) measured from the cross-correlations rather than the cross-correlations themselves. One method is to determine if the travel time field computed for a single central station varies smoothly spatially (e.g., Fig. 5.13). Another is to determine if the measurements at a given period can be fit well with a smooth dispersion map. Figure 5.14 presents example histograms of the misfit of Rayleigh wave phase speed measurements across China at different periods to a set of smooth dispersion maps that form the basis for a 3D model (Shen et al., 2016). The standard deviations of such phase travel time

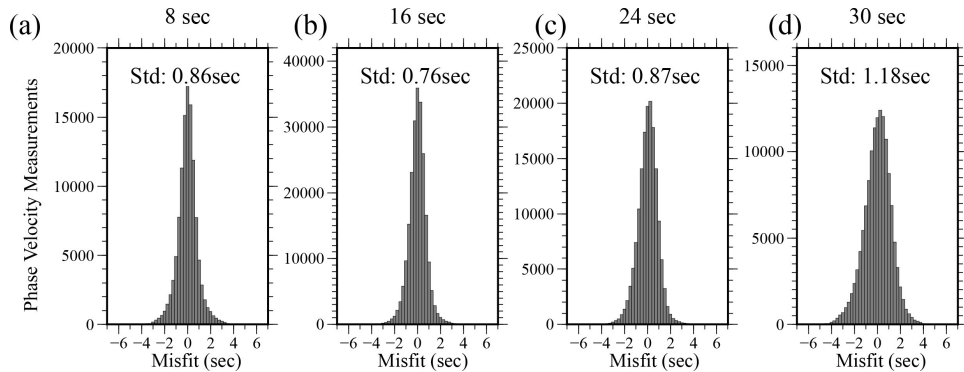


Figure 5.14 Examples of misfit histograms defined as observed Rayleigh wave phase times minus predicted phase times (in sec) computed from an estimated phase speed map at different periods across China. The standard deviation of each misfit distribution is presented in each panel. This figure is adapted from Fig. 2 of Shen et al. (2016).

misfits are typically about 1 sec (but are higher for group times). Measurements that are fit much worse than this (for example, worse than about 3 standard deviations) are typically rejected. Such misfit histograms plotted for measurements in which a particular station participates, are also useful to identify problems with stations such as timing errors, location errors, and instrument response errors (e.g., Zhou et al., 2012), which are either corrected or the station is removed from the experiment. We sometimes refer to the ability of a smooth dispersion maps to fit the dispersion measurements as a “simplicity” criterion.

Information about measurement errors and in inferred quantities such as dispersion maps and earth models, is contained in the tests represented by the above criteria, particularly tests of stability, self-consistency, and cross-consistency. As discussed in section 6.2, ideally we prefer to use cross-consistency to constrain errors in dispersion maps rather than other criteria that provide information about errors in the dispersion measurements themselves. But all are relevant both to the selection of data retained in the experiment and to the assessment of uncertainties in the inferred quantities.

5.6.2 Quantifying Uncertainty

The necessary conditions discussed in section 6.1 provide circumstantial evidence about the reliability of a given cross-correlation and measurements obtained from it (e.g., surface wave dispersion). This evidence is useful for the acceptance or rejection of data in the experiment. Once accepted in an

experiment, however, one wishes to assess the data's reliability and quantify that assessment as data uncertainties. Thus, we take up Question 2 here.

There are four levels of uncertainty worth mentioning: (1) errors in the cross-correlations themselves, (2) errors in measurements obtained on the cross-correlations (e.g. group and phase speed measurements), (3) errors in surface wave dispersion maps, and (4) errors in structural models of the Earth. We will not consider here the first and last of these, but will focus on the assessment of uncertainties in dispersion measurements and dispersion maps, which are commonly produced intermediate products in the construction of structural models of the Earth. As discussed in section 6.1, the stability, repeatability, and self-consistency of measurements are useful tools to quantify the uncertainty of dispersion measurements. In particular, the spatial (e.g., Fig. 5.9) and temporal (notably seasonal) variability of dispersion measurements, the variation between measurements obtained on positive and negative lags, and the misfit produced by dispersion maps (e.g., Fig. 5.14) have all proven useful to quantify dispersion measurement uncertainty. SNR has also been shown to be a useful proxy so that measurement uncertainty can be inferred from it.

Dispersion maps, however, are what are most commonly used in inversions for 3D structural models rather than raw dispersion measurements. Uncertainty estimates in tomographic maps can be produced either in the context of a linearized tomographic inversion in which estimates of data uncertainties are propagated to model uncertainties (i.e., dispersion maps) in standard ways (e.g., Barmin et al., 2001) or via non-tomographic, spatially localized methods such as eikonal (Lin et al., 2009) and Helmholtz tomography (Lin and Ritzwoller, 2011) in which no forward matrix is constructed, decomposed, or inverted. As instrumental seismology has advanced, the installation of arrays at which the localized non-tomographic methods can be applied is an increasingly common practice. For this reason, we discuss here uncertainties in the context of such array-based methods, acknowledging that the methods are not friendly to spatial gaps in station coverage.

Eikonal tomography is based exclusively on observed travel time surfaces like that shown for the 24 s Rayleigh wave in Figure 5.13, although separate maps are constructed for each period and for each central station. In Helmholtz tomography, similar observed amplitude maps are used to apply a finite frequency correction. Because absolute amplitude information is commonly lost in ambient noise data processing, such amplitude based corrections are typically not applied in ambient noise studies. As described by Lin et al. (2009), based on the eikonal equation, the local phase speed and direction of wave propagation can be inferred from the gradient of the local

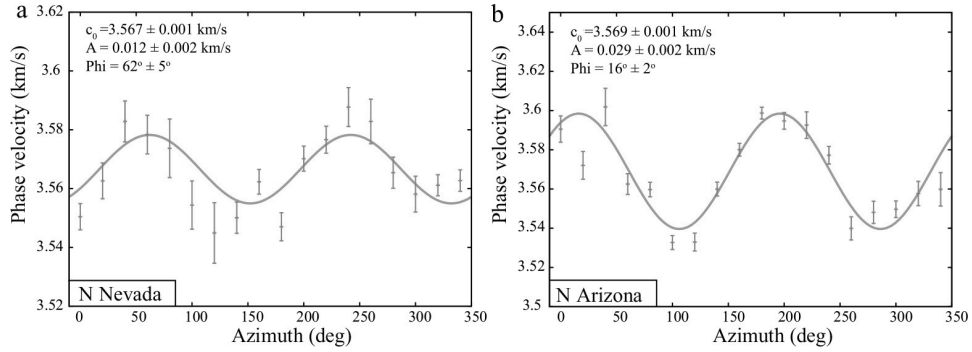


Figure 5.15 Phase speed as a function of inter-station azimuth averaged in each 20° bin for the 24 s Rayleigh wave are plotted as error bars that represent the RMS variation in each bin. The example points are in (a) Nevada (242°E , 42°N) and (b) Arizona (250°E , 36°N). The best-fitting 2ψ curve (eqn. (5.18)) is presented as the solid line in each panel. Estimated values with 1 standard deviation errors for c_0 , A and ϕ are listed at upper left in each panel. The 2ψ component of anisotropy is clear in both panels. This figure is adapted from Fig. 4 of Ritzwoller et al. (2011).

travel time. Using maps from many central stations allows the observation of the mean and azimuthal variation of local phase speed, as illustrated Figure 5.15. Following Smith and Dahlen (1973), these quantities can be modeled as a function of azimuthal angle, ψ , as follows:

$$c(\psi) \approx c_0 + A \cos[2(\psi - \phi)], \quad (5.18)$$

in which the c_0 represents the local average of the isotropic component of phase speed and A and ϕ are mean estimates of the amplitude and fast-axis direction of azimuthal anisotropy. An example of such mean estimates is presented in Figure 5.16 for the 24 s Rayleigh wave.

The error bars in Figure 5.15 represent the variation of the measurements in each azimuthal bin. They are, therefore, related to stability, repeatability, and self-consistency as discussed in section 6.1. If they are interpreted as one standard deviation Gaussian errors, they can be transformed to uncertainties in the quantities c_0 , A , and ϕ in a standard way. Figure 5.17 illustrates such error estimates on isotropic and anisotropic dispersion curves below 25 s period for Rayleigh waves. Such estimates may not capture the potential effects of systematic errors, however.

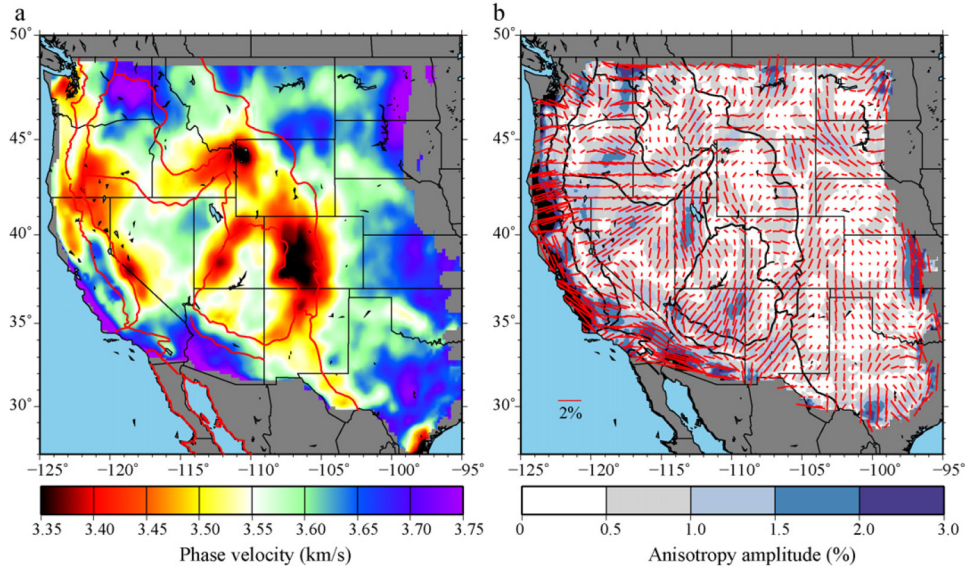


Figure 5.16 (a) The 24 s Rayleigh wave isotropic phase speed map taken from ambient noise by averaging all local phase speed measurements at each point on the map (b) The amplitudes and fast directions of the 2ψ component of the 24 s Rayleigh wave phase velocities. The amplitude of anisotropy is identified with the length of the bars, which point in the fast-axis direction, and is color-coded in the background. At 24 s period, Rayleigh wave anisotropy reflects a combination of crust and uppermost mantle. This figure is adapted from Fig. 5 of Ritzwoller et al. (2011).

5.6.3 Assessing Systematic Error

The necessary conditions discussed in sections 6.1 and 6.2 provide indicators that measure the variance in the cross-correlations, measurements made from them, and inferences drawn from those measurements. Such indicators do not guarantee against systematic error. To assess the extent of systematic error, or bias, it is useful to consider sufficient conditions that may link cross-correlations and Green's functions.

We define a sufficient condition X as follows.

Sufficient Condition: If criterion X is satisfied, then an ensemble-averaged (temporally-stacked) cross-correlation $\Gamma_{ij}(t)$ computed from recordings observed at stations i and j will be a good approximation to the Green's function $G_{ij}(t)$ between the stations, consistent with equation (5.5).

Well formulated sufficient conditions, as distinct from necessary conditions, are powerful as they guarantee that a cross-correlation reliably approximates

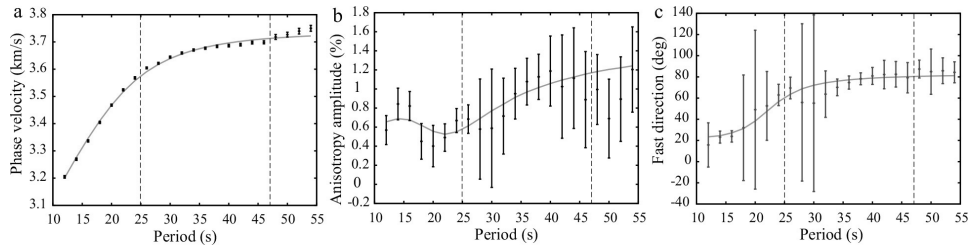


Figure 5.17 Isotropic and azimuthally anisotropic dispersion curves got a point in northern Nevada. Only ambient noise measurements are used at periods below 25 s, ambient noise and earthquake measurements are averaged between 25 s and 45 s period, and only earthquake measurements are used above 45 s period. Phase velocity is presented in km/s, anisotropy amplitude in percent, and the fast direction of anisotropy in degrees east of north. Measurement uncertainties are presented with one standard deviation error bars. The best-fitting curves based on the isotropic and anisotropic inversions are presented as the continuous line in each panel. This figure is adapted from Fig. 8 of Ritzwoller et al. (2011).

a Green's function. But such conditions are hard to come by. We consider only one here – the comparison of dispersion measurements and maps obtained from ambient noise to those obtained from earthquakes. Such comparisons cannot be performed at every period because earthquake results do not extend to as short of periods as ambient noise results. This is one of the ways ambient noise tomography has provided new information about the Earth (Chapters 7 and 8 (Shapiro, 2018; Nakata and Nishida, 2018)). Conversely, earthquake results often extend to longer periods than ambient noise results. Consequently, these two sources of information are complementary and better used together than independently (e.g., Yang et al., 2008, and many others).

Both Figures 5.17 and 5.18 present comparisons between phase speeds derived from ambient noise and earthquakes. First, Figure 5.18 shows Rayleigh wave dispersion maps at 30 s period, which is in the band of overlap between the methods. There are differences in detail between these maps, but a quantitative comparison does not indicate systematic differences. The result of the similarity of these different measurements is that they can be used simultaneously, as in the isotropic and anisotropic dispersion curves presented in Figure 5.17 in which in the period band between 25 and 45 s ambient noise and earthquake dispersion measurements are averaged.

Sufficient condition comparisons such as those we present here provide great confidence in ambient noise cross-correlations to deliver unbiased information about the crust and uppermost mantle. However, such comparisons

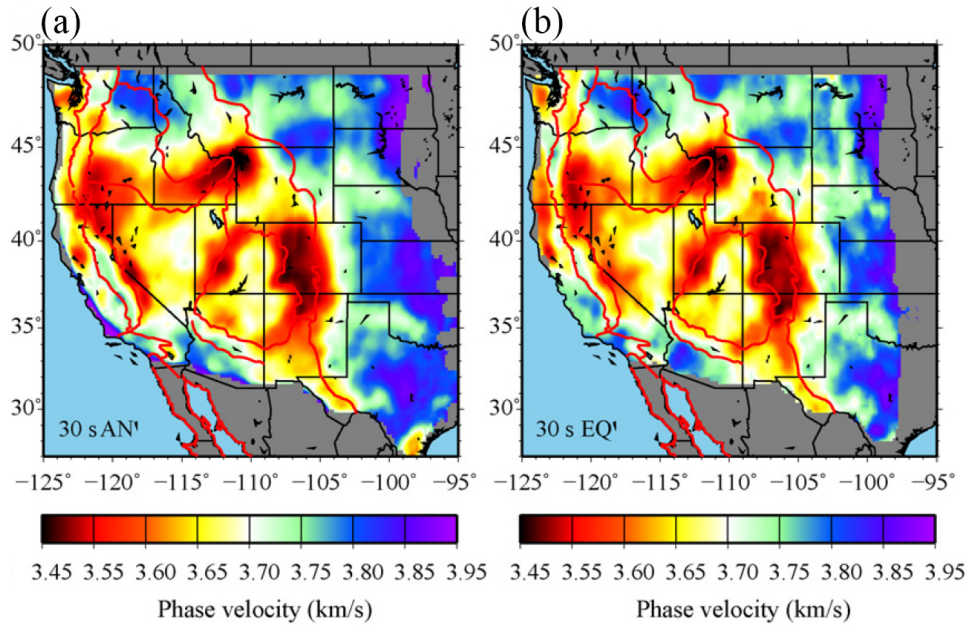


Figure 5.18 (a) Isotropic maps for the 30 s period Rayleigh wave phase speed observed via eikonal tomography applied to ambient noise data. (b) A similar map for comparison constructed by eikonal tomography applied to earthquake data. This figure is adapted from Fig. 7 of Ritzwoller et al. (2011).

involve a highly processed product of ambient noise data processing and tomography. Consequently, unlike the necessary conditions discussed earlier in this section, sufficient conditions tend to cause the cross-correlations to stand or fall together and do not test a single or small subset of the cross-correlations or measurements.

5.7 Recent Developments in Ambient Noise Data Processing

In this section, we briefly review some recently developed methods designed to amplify or extend the methods described in previous sections. It is impossible to cover all the studies related to this topic and we, therefore, only list a few in several different categories that we consider to be representative. We divide these methods into four categories:

- (1) Preprocessing procedures applied before cross-correlation,

- (2) De-noising techniques applied to cross-correlation waveforms and advanced stacking schemes,
- (3) Post-processing methods applied to the stacked cross-correlation data, and
- (4) Advanced seismic interferometry methods.

Categories (1)-(3) are the techniques that are designed to be applied in the context of conventional seismic interferometry for seismic tomography, in which surface wave arrivals emitted from one virtual source are recorded at one station. Category (4), however, includes sophisticated interferometric methods that go beyond conventional approaches.

5.7.1 Preprocessing Techniques Applied Before Cross-Correlation

Although the time and frequency domain weighting or normalization techniques described above have proven to be quite useful, they have some drawbacks and researchers have proposed new methods to enhance their performance. We present two examples here.

Prieto et al. (2009) used complex coherency (see section 2 above for a definition), which preserves the amplitude information in ambient noise. They applied this technique to data from 154 broadband seismic stations in southern California and received a similar Q model as earlier work based on earthquakes (Yang and Forsyth, 2008). Following this work, Seats et al. (2012) demonstrated that a faster convergence to empirical Green's functions can be achieved by using short duration overlapped time windows rather than longer, non-overlapped time windows for cross-correlation, the so-called Welch's method (Welch, 1967).

Inspired by Gallot et al. (2012) and Carrière et al. (2014), Seydoux et al. (2017) developed an array-based technique to equalize noise energy coming from different azimuths. The cross-spectrum matrix defined by equation (5.1) earlier in the chapter, defines a positive semi-definite Hermitian matrix, \mathbf{G} , termed the array covariance matrix by Seydoux et al. (2017). It can be diagonalized as $\mathbf{G} = \mathbf{\Psi}\mathbf{\Delta}\mathbf{\Psi}^\dagger$, where $\mathbf{\Delta} = \text{diag}(\lambda_1, \lambda_2, \dots)$ is the diagonal matrix formed by the non-negative eigenvalues λ_i and where $\mathbf{\Psi}$ is the matrix of the eigenvectors. The authors construct an equalized covariance (cross-spectrum) matrix, $\hat{\mathbf{G}}$, such that $\hat{\mathbf{G}} = \mathbf{\Psi}\hat{\mathbf{\Delta}}\mathbf{\Psi}^\dagger$. $\hat{\mathbf{\Delta}}$ contains the equalized eigenvalues, obtained by setting all the eigenvalues $\lambda_i = 1$ when $i \leq L$ and $\lambda_i = 0$ otherwise. The index L is the cut-off for eigenvectors that are considered as noise-related and should be discarded. By applying this tech-

nique to both synthetic and real datasets, the authors demonstrated that the symmetry of cross-correlation waveforms can be enhanced and precursory noise suppressed. The beam energy of the processed array data also indicates a more isotropic distribution of sources.

5.7.2 De-Noising Techniques Applied to Cross-Correlation Waveforms and Advanced Stacking Schemes

Another branch of data processing techniques for ambient noise is designed to be applied after the cross-correlation computation. Typically, finalized cross-correlation waveforms for seismic tomography are obtained by stacking all the daily (or hourly depending on the length of the windows chosen for cross-correlation) correlation data. The stacking scheme can be improved by selecting signals wisely and we summarize several ideas here to improve this selection. All the methods mentioned in this section have one thing in common: they all assume that coherent signals are contained in each daily cross-correlation and attempt to extract that signal while discarding the incoherent noise using an intelligent selection criterion.

By transforming the daily records into the frequency-time domain based on the S-transform (Stockwell et al., 1996), Baig et al. (2009) proposed to construct a weight function for each octave and time range. This weight function can be designed to optimize the coherence in phase/amplitude for daily cross-correlation data, and thus could serve as a filter to de-noise the stacked cross-correlation waveform. The authors applied the technique to real data recorded in California and observed that more meaningful Rayleigh and Love wave travel time measurements were obtained. The method of Baig et al. (2009) was later called time-frequency phase-weighted stacking (tf-PWS) by Schimmel et al. (2011), who proposed to use a different version of S-transform to perform the weighted stacking scheme. Schimmel et al. (2011) also defined a new type of cross-correlation, the phase cross-correlation (PCC). Different from the conventional cross-correlation, the PCC is more sensitive to small amplitude signals. Schimmel et al. (2011) applied both the tf-PWS and PCC methods to synthetic and real data and observed enhanced SNR in the cross-correlation waveforms.

Liu et al. (2016) proposed another advanced stacking scheme based on a bootstrap resampling approach. They performed a statistical analysis of the daily (or hourly/monthly depending on the time window length) cross-spectra to identify outliers to discard during stacking. The analysis also yields the variance of the cross-spectra and provides a probabilistic determination of the reliability of the stacked cross-spectrum. Figure 10 in Liu

et al. (2016) compares a quality-controlled stacked cross-spectrum with raw stacked cross-spectra, along with estimates of uncertainties for each data point. The noise in the finalized cross-spectrum can be significantly reduced via this method to discard outliers.

Another way of “selecting” data is to de-noise the cross-correlation waveform before stacking. Stehly et al. (2011) proposed the use of a curvelet denoising filter to be applied to the daily cross-correlation before stacking. The method is based on the idea that the wavefront can be sparsely represented with curvelet coefficients. Given the 2D image of the daily cross-correlation, the sum of all the daily records yields an empirical Green’s function with a low SNR. To perform the de-noising, the 2D image is transformed into the 2D curvelet domain. Because the signals in the original 2D image construct a 2D planar wavefront, which can be sparsely represented by a subset of the curvelet coefficients with relatively large values, the large number of small curvelet coefficients can be discarded. Then by performing an inverse curvelet transform, the authors received de-noised cross-correlation data shown in Figure 4c in their paper. The stacked cross-correlation data from the de-noised 2D image has an improved SNR. The authors also proposed a more sophisticated filtering scheme by using the original stacked cross-correlation waveform as a reference for the selection of the curvelet coefficients. They applied this technique to get more reliable empirical Green’s functions whose coda waves were used to monitor seismic wave velocity changes associated with the Mw 7.9 Wenchuan earthquake (Stehly et al., 2015).

5.7.3 Post-processing methods applied to the stacked cross-correlation data

After the stacked cross-correlation waveforms are generated, researchers typically perform seismic tomography using the travel time measurements obtained on the correlation waveforms. However, some additional information can also be retrieved from the cross-correlation data using various post-processing approaches, of which we mention a couple here.

van Wijk et al. (2011) and Takagi et al. (2014) proposed to use cross terms of the ambient noise Green’s tensor to separate body waves from Rayleigh waves. Their idea is based on the fact that, theoretically, the RZ and ZR components of the cross-correlation tensors are time symmetric for Rayleigh waves while time anti-symmetric for P-waves for isotropic media. The use of $(ZR-RZ)/2$ may suppress the P-wave and reduce noise precursory to the

Rayleigh wave. Similarly, $(ZR+RZ)/2$ will accentuate the P-waves at the expense of the Rayleigh waves.

Another interesting post-processing procedure is to compute the correlation of the coda of the cross-correlation, which is referred to as C3 (Stehly et al., 2008), in contrast with traditional cross-correlations of ambient noise (C1). Ideally, the empirical Green's function between a station-pair should include all the propagation effects between the two stations. Thus, not only the ballistic waves but also the coda should be included in the original cross-correlation. Because the coda wavefield is typically diffuse, empirical Green's functions can be extracted by correlating the coda window of the noise correlation. In fact, before the era of ambient noise tomography, Campillo and Paul (2003) discovered that the cross-correlation of earthquake coda can yield empirical Green's functions. Compared with the ambient noise cross-correlation function, the C3 function may be more symmetric if the stations used for the computation are more evenly distributed geographically. Moreover, Zhang and Yang (2013) proved that C3 is more suitable for the extraction of attenuation information compared with the traditional noise cross-correlation.

A potentially much more significant advantage of C3 over traditional ambient noise correlation is that it can be used to extract empirical Green's functions between station-pairs even when the two stations are not operating simultaneously. This requires that there are some other stations that have operation times that overlap those two asynchronous ones. Ma and Beroza (2012) demonstrated the feasibility of this using data from southern California. A potential downside of the use of C3 is that the coda tends to be more band-limited than the Rayleigh wave observed with C1 and the recovery of meaningful empirical Green's functions is more difficult than with the use of C1.

5.7.4 Advanced seismic interferometric theories and methods

Several researchers have proposed more advanced seismic interferometry theories that go beyond approaches that have been applied previously. We briefly introduce two of them.

As mentioned previously in this chapter, precursory noise can emerge in ambient noise cross-correlation waveforms when the distribution of noise sources differs significantly from azimuthal homogeneity. Conventionally, observers attempt to eliminate or suppress these spurious arrivals. In fact, traditional ambient noise tomographic inversions have been performed by assuming the only meaningful arrival is the ballistic wave emitted from one

station (or virtual source) and recorded by another station. Recently, Fichtner et al. (2017) developed a more general seismic interferometry theory for cross-correlations that can use the precursory noise to constrain Earth structure (see also Section 5 of Fichtner and Tsai, 2018). Figure 13 of Fichtner et al. (2017) illustrates that the sensitivity kernels for different waveform windows, including precursory arrivals, can be used to constrain the Earth. Fichtner's theory is sophisticated and it is not trivial to apply the method to real data. However, at the very least, it demonstrates the feasibility of using precursory arrivals from cross-correlation data for seismic imaging.

Another advanced seismic interferometry theory that goes beyond conventional cross-correlation approaches has been developed by Kees Wapenaar and his collaborators. These methods are designed to improve the performance of ambient noise cross-correlation in the presence of highly inhomogeneously distributed noise sources. Wapenaar and his co-workers developed a new type of computation called multidimensional deconvolution (MDD) and proved theoretically that this procedure can guarantee the retrieval of accurate empirical Green's functions even when the source distribution is one-sided (Wapenaar and van der Neut, 2010; Wapenaar et al., 2011). Figures 2 and 3 in Wapenaar et al. (2011) demonstrate the improvement that MDD can achieve compared with cross-correlation. An application of this technique to real data for surface waveform retrieval was presented by van Dalen et al. (2015). Although the method appears to be promising, MDD also has some limitations. To retrieve an empirical Green's function for a station pair, a regular array of receivers is required to construct the so-called point spread function (PSF) for the deconvolution computation (see Wapenaar and van der Neut (2010) for more detail). The MDD is computationally more expensive than cross-correlation and the matrix inversion in the deconvolution may be unstable. Despite these caveats, the MDD theory provides a possible new path to retrieve more reliable Green's functions from ambient noise.

5.8 Conclusions

This chapter presents a discussion of some of the practical issues involved with processing ambient noise recorded at two stations and cross-correlating such recordings to recover reliable estimated Green's functions between the stations, at least for the surface wave parts of the Green's function. Our focus is on regional scale broadband ambient noise seismology, which delivers

information at lateral resolutions from 10s to 100s of km about the crust and uppermost mantle.

A number of data processing variables affect the resulting cross-correlations, including the length of the records in the time domain that are cross-correlated, and the nature of the normalization of records in the time and frequency domains. We discuss how to obtain surface wave dispersion (group and phase speed) measurements in the time domain. We also discuss the reduction of tilt and compliance noise, which is required in an ocean bottom setting.

A significant part of ambient noise data processing is the selection and rejection of particular cross-correlations. We list a number of useful criteria on which to base such decisions, which we present as necessary conditions to be satisfied for cross-correlations to provide reliable approximations to Green's functions. These conditions include the SNR of the cross-correlations, their temporal stability (particularly over seasons), the level of precursory noise, the self-similarity of measurements obtained on the cross-correlations over time and frequency, and their correspondence to other cross-correlations. The stability, repeatability, and self-consistency of dispersion measurements are useful tools to quantify the uncertainty of dispersion measurements. Array-based methods are particularly useful to estimate uncertainties in dispersion maps (e.g., eikonal tomography).

The ultimate question is: Why should we believe that ambient noise provides reliable information about the Earth? Part of this question is answered with the uncertainty estimates discussed in the previous paragraph, but only part. Such uncertainty estimates primarily quantify the variability of the measurements, which does not include an assessment of systematic errors. The principal reason we believe that ambient noise does not provide a biased estimator, at least in many circumstances, is that ambient noise results can be compared with earthquake results. For example, phase velocity maps from ambient noise and earthquake tomography can be compared in detail. When this has been done carefully, bias has been seen to be small and reduces with the length of ambient noise observation and the number of earthquakes.

Further improvements in ambient noise data processing are needed and we summarize a few recent amplifications and extensions of the methods presented in this chapter. Particular needs include the fact that Love waves are narrower band than Rayleigh waves on continents and are very hard to observe in ocean bottom settings using OBS data. The reader is encouraged to remember that what we seek are observational methods to yield broadband, low variance, and unbiased information about the Earth and,

preferably, methods that will speed convergence and thus reduce observation time. Ambient noise seismology remains a young discipline, and readers are encouraged to view the current state-of-the-art as merely the starting point to supersede with own creative work in ambient noise seismology.

Acknowledgements

The authors are grateful to two anonymous reviewers and Nori Nakata for criticisms that helped to improve this chapter. Much of the work on which this chapter rests has been supported by grants from the US National Science Foundation and the US Department of Defense. The facilities of the IRIS Data Management System were used to access all of the data used in this study. The IRIS DMS is funded through the US National Science Foundation under Cooperative Agreement EAR-0552316. The authors are also grateful to the Cascadia Initiative Expedition Team for acquiring the Amphibious Array Ocean Bottom Seismograph data and appreciate the open data policy that makes these data available. This work utilized the Janus supercomputer, which is supported by the National Science Foundation (award number CNS-0821794), the University of Colorado Boulder, the University of Colorado Denver, and the National Center for Atmospheric Research. The Janus supercomputer is operated by the University of Colorado at Boulder.

References

- Aki, K. 1957. Space and Time Spectra of Stationary Stochastic Waves, with Special Reference to Microtremors. *Bull. Earthq. Res. Inst.*, **35**, 415–456.
- Ardhuin, F., Gualtieri, L., and Stutzmann, E. 2018. Physics of ambient noise generation by ocean waves. Pages — of: Nakata, N., Gualtieri, L., and Fichtner, A. (eds), *Seismic Ambient Noise*. Cambridge University Press, Cambridge, UK.
- Baig, A. M., Campillo, M., and Brenguier, F. 2009. Denoising seismic noise cross correlations. *J. Geophys. Res.*, **114**, B08310.
- Ball, J. S., Sheehan, A. F., Stachnik, J. C., Lin, F.-C., and Collins, J. A. 2014. A joint Monte Carlo analysis of seafloor compliance, Rayleigh wave dispersion and receiver functions at ocean bottom seismic stations offshore New Zealand. *Geochem. Geophys. Geosyst.*, **15**, 5051–5068.
- Barmin, M. P., Ritzwoller, M. H., and Levshin, A. L. 2001. A fast and reliable method for surface wave tomography. *Pure Appl. Geophys.*, **158**, 1351–1375.
- Bell, S. W., Forsyth, D. W., and Ruan, Y. 2015. Removing noise from the vertical component records of ocean-bottom seismometers: Results from year one of the Cascadia Initiative. *Bull. Seismol. Soc. Am.*, **105**(1), 300–313.

- Bensen, G. D., Ritzwoller, M. H., Barmin, M. P., Levshin, A. L., Lin, F., Moschetti, M. P., Shapiro, N. M., and Yang, Y. 2007. Processing seismic ambient noise data to obtain reliable broad-band surface wave dispersion measurements. *Geophys. J. Int.*, **169**, 1239–1260.
- Bowden, D. C., Kohler, M. D., Tsai, V. C., and Weeraratne, D. S. 2016. Offshore southern California lithospheric velocity structure from noise cross-correlation functions. *J. Geophys. Res.*, **121**(5), 3415–3427.
- Bracewell, R. N. 1978. *The Fourier transform and its applications*. 2 edn. McGraw-Hill.
- Campillo, M., and Paul, A. 2003. Long-range correlations in the diffuse seismic coda. *Science*, **299**, 547–549.
- Carrière, O., Gerstoft, P., and Hodgkiss, W. S. 2014. Spatial filtering in ambient noise interferometry. *J. Acoust. Soc. Am.*, **135**(3), 1186–1196.
- Crawford, W. C., and Webb, S. C. 2000. Identifying and removing tilt noise from low-frequency (<0.1 Hz) seafloor vertical seismic data. *Bull. Seismol. Soc. Am.*, **90**(4), 952–963.
- Dolenc, D., Romanowicz, B., Uhrhammer, R., McGill, P., Neuhauser, D., and Stakes, D. 2007. Identifying and removing noise from the Monterey ocean bottom broadband seismic station (MOBB) data. *Geochem. Geophys. Geosyst.*, **8**(2), Q02005.
- Duennebieer, F. K., and Sutton, G. H. 1995. Fidelity of ocean bottom seismic observations. *Marine Geophys. Res.*, **17**, 535–555.
- Ekström, G., Geoffrey A. Abers, and Webb, S. C. 2009. Determination of surface-wave phase velocities across USArray from noise and Aki's spectral formulation. *Geophys. Res. Lett.*, **36**, L18301.
- Fichtner, A., and Tsai, V. 2018. Theoretical foundations of noise interferometry. Pages — of: Nakata, N., Gualtieri, L., and Fichtner, A. (eds), *Seismic Ambient Noise*. Cambridge University Press, Cambridge, UK.
- Fichtner, A., Stehly, L., Ermert, L., and Boehm, C. 2017. Generalized interferometry – I: theory for interstation correlations. *Geophys. J. Int.*, **208**, 603–638.
- Gallot, T., Catheline, S., Roux, P., and Campillo, M. 2012. A passive inverse filter for Green's function retrieval. *J. Acoust. Soc. Am.*, **131**(1), EL21–EL27.
- Gao, H., and Shen, Y. 2015. A preliminary full-wave ambient-noise tomography model spanning from the Juan de Fuca and Gorda spreading centers to the Cascadia volcanic arc. *Seismol. Res. Lett.*, **86**(5), 1253–1260.
- Harmon, N., Forsyth, D., and Webb, S. 2007. Using ambient seismic noise to determine short-period phase velocities and shallow shear velocities in young oceanic lithosphere. *Bull. Seismol. Soc. Am.*, **97**(6), 2009–2023.
- Levshin, A. L., and Ritzwoller, M. H. 2001. Automated detection, extraction, and measurement of regional surface waves. *Pure Appl. Geophys.*, **158**, 1531–1545.
- Levshin, A. L., Yanovskaya, T. B., Lander, A. V., Bukchin, B. G., Barmin, M. P., Ratnikova, L. I., and Its, E. N. 1989. *Seismic surface waves in laterally inhomogeneous Earth*. Kluwer. Publ.
- Lin, F.-C., and Ritzwoller, M. H. 2011. Helmholtz surface wave tomography for isotropic and azimuthally anisotropic structure. *Geophys. J. Int.*, **186**, 1104–1120.
- Lin, F.-C., Ritzwoller, M. H., Townend, J., Bannister, S., and Savage, M. K. 2007. Ambient noise Rayleigh wave tomography of New Zealand. *Geophys. J. Int.*, **170**, 649–666.

- Lin, F.-C., Moschetti, M. P., and Ritzwoller, M. H. 2008. Surface wave tomography of the western United States from ambient seismic noise: Rayleigh and Love wave phase velocity maps. *Geophys. J. Int.*, **173**, 281–298.
- Lin, F.-C., Ritzwoller, M. H., and Snieder, R. 2009. Eikonal tomography: surface wave tomography by phase front tracking across a regional broad-band seismic array. *Geophys. J. Int.*, **177**, 1091–1110.
- Lin, F.-C., Ritzwoller, M. H., Yang, Y., Moschetti, M. P., and Fouch, M. J. 2011. Complex and variable crustal and uppermost mantle seismic anisotropy in the western United States. *Nature Geosci.*, **4**, 55–61.
- Liu, X., Ben-Zion, Y., and Zigone, D. 2016. Frequency domain analysis of errors in cross-correlations of ambient seismic noise. *Geophys. J. Int.*, **207**, 1630–1652.
- Luo, Y., Yang, Y., Xu, Y., Xu, H., Zhao, K., and Wang, K. 2015. On the limitations of interstation distances in ambient noise tomography. *Geophys. J. Int.*, **201**, 652–661.
- Ma, S., and Beroza, G. C. 2012. Ambient-field Green’s functions from asynchronous seismic observations. *Geophys. Res. Lett.*, **39**, L06301.
- McNamara, D., and Boaz, R. 2018. Visualization of the Seismic Ambient Noise Spectrum. Pages — of: Nakata, N., Gualtieri, L., and Fichtner, A. (eds), *Seismic Ambient Noise*. Cambridge University Press, Cambridge, UK.
- Moschetti, M. P., Ritzwoller, M. H., Lin, F., and Yang, Y. 2010. Seismic evidence for widespread western-US deep-crustal deformation caused by extension. *Nature*, **464**, 885–890.
- Nakata, N., and Nishida, K. 2018. Body wave exploration. Pages — of: Nakata, N., Gualtieri, L., and Fichtner, A. (eds), *Seismic Ambient Noise*. Cambridge University Press, Cambridge, UK.
- Prieto, G. A., Lawrence, J. F., and Beroza, G. C. 2009. Anelastic earth structure from the coherency of the ambient seismic field. *J. Geophys. Res.*, **114**, B07303.
- Prieto, G. A., Denolle, M., Lawrence, J. F., and Beroza, G. C. 2011. On amplitude information carried by the ambient seismic field. *C.R. Geosci.*, **343**, 600–614.
- Ritzwoller, M. H., Lin, F.-C., and Shen, W. 2011. Ambient noise tomography with a large seismic array. *C. R. Geoscience*, **343**, 558–570.
- Schimmel, M., Stutzmann, E., and Gallart, J. 2011. Using instantaneous phase coherence for signal extraction from ambient noise data at a local to a global scale. *Geophys. J. Int.*, **184**(1), 494–506.
- Seats, K. J., Lawrence, J. F., and Prieto, G. A. 2012. Improved ambient noise correlation functions using Welch’s method. *Geophys. J. Int.*, **188**, 513–523.
- Seydoux, L., de Rosny, J., and Shapiro, N. M. 2017. Pre-processing ambient noise cross-correlations with equalizing the covariance matrix eigenspectrum. *Geophys. J. Int.*, **210**, 1432–1449.
- Shapiro, N. 2018. Applications with surface waves extracted from ambient seismic noise. Pages — of: Nakata, N., Gualtieri, L., and Fichtner, A. (eds), *Seismic Ambient Noise*. Cambridge University Press, Cambridge, UK.
- Shapiro, N. M., and Ritzwoller, M. H. 2002. Monte-Carlo inversion for a global shear-velocity model of the crust and upper mantle. *Geophys. J. Int.*, **151**, 88–105.
- Shapiro, N. M., Ritzwoller, M. H., and Bensen, G. D. 2006. Source location of the 26 sec microseism from cross-correlations of ambient seismic noise. *Geophys. Res. Lett.*, **33**, L18310.
- Shen, W., Ritzwoller, M. H., Kang, D., Kim, Y., Lin, F.-C., Ning, J., Wang, W., Zheng, Y., and Zhou, L. 2016. A seismic reference model for the crust and

- uppermost mantle beneath China from surface wave dispersion. *Geophys. J. Int.*, **206**, 954–979.
- Shen, Y., Ren, Y., Gao, H., and Savage, B. 2012. An improved method to extract very-broadband empirical Green's functions from ambient seismic noise. *Bull. Seismol. Soc. Am.*, **102**(4), 1872–1877.
- Smith, M. L., and Dahlen, F. A. 1973. The azimuthal dependence of Love and Rayleigh wave propagation in a slightly anisotropic medium. *J. Geophys. Res.*, **78**(17), 3321–3333.
- Snieder, R. 2004. Extracting the Green's function from the correlation of coda waves: A derivation based on stationary phase. *Phys. Rev. E*, **69**, 046610.
- Stehly, L., Campillo, M., and Shapiro, N. M. 2007. Traveltime measurements from noise correlation: stability and detection of instrumental time-shifts. *Geophys. J. Int.*, **171**, 223–230.
- Stehly, L., Campillo, M., Froment, B., and Weaver, R. L. 2008. Reconstruction Green's function by correlation of the coda of the correlation (C^3) of ambient seismic noise. *J. Geophys. Res.*, **113**, B11306.
- Stehly, L., Cupillard, P., and Romanowicz, B. 2011. Towards improving ambient noise tomography using simultaneously curvelet denoising filteres and SEM simulations of seismic ambient noise. *C. R. Geoscience*, **343**, 591–599.
- Stehly, L., Froment, B., Campillo, M., Liu, Q. Y., and Chen, J. H. 2015. Monitoring seismic wave velocity changes associated with the M_W 7.9 Wenchuan earthquake: increasing the temporal resolution using curvelet filters. *Geophys. J. Int.*, **201**, 1939–1949.
- Stockwell, R. G., Mansinha, L., and Lowe, R. P. 1996. Localization of the complex spectrum: The S transform. *IEEE Trans Signal Process*, **44**(4), 998–1001.
- Takagi, R., Nakahara, H., Kono, T., and Okada, T. 2014. Separating body and Rayleigh waves with cross terms of the cross-correlation tensor of ambient noise. *J. Geophys. Res.*, **119**, 2005–2018.
- Tian, Y., and Ritzwoller, M. H. 2015. Directionality of ambient noise on the Juan de Fuca plate: implications for source locations of the primary and secondary microseisms. *Geophys. J. Int.*, **201**, 429–443.
- Tian, Y., and Ritzwoller, M. H. 2017. Improving ambient noise cross-correlations in the noisy ocean bottom environment of the Juan de Fuca plate. *Geophys. J. Int.*, **210**, 1787–1805.
- Tian, Y., Shen, W., and Ritzwoller, M. H. 2013. Crustal and uppermost mantle shear velocity structure adjacent to the Juan de Fuca Ridge from ambient seismic noise. *Geochem. Geophys. Geosyst.*, **14**(8), 3221–3233.
- van Dalen, K. N., Mikesell, T. D., Ruigrok, E. N., and Wapenaar, K. 2015. Retrieving surface waves from ambient seismic noise using seismic interferometry by multidimensional deconvolution. *J. Geophys. Res.*, **120**, 994–961.
- van Wijk, K., Mikesell, T. D., Schulte-Pelkum, V., and Stachnik, J. 2011. Estimating the Rayleigh-wave impulse response between seismic stations with the cross terms of the Green tensor. *Geophys. Res. Lett.*, **38**, L16301.
- Wapenaar, K., and van der Neut, J. 2010. A representation for Green's function retrieval by multidimensional deconvolution. *J. Acoust. Soc. Am.*, **128**(6), EL366–EL371.
- Wapenaar, K., van der Neut, J., Ruigrok, E., Draganov, D., Hunziker, J., Slob, E., Thorbecke, J., and Snieder, R. 2011. Seismic interferometry by crosscorrelation and by multidimensional deconvolution: a systematic comparison. *Geophys. J. Int.*, **185**, 1335–1364.

- Webb, S. C. 1988. Long-period acoustic and seismic measurements and ocean floor currents. *IEEE J Ocean Eng*, **13**(4), 263–270.
- Webb, S. C., and Crawford, W. C. 1999. Long-period seafloor seismology and deformation under ocean waves. *Bull. Seismol. Soc. Am.*, **89**(6), 1535–1542.
- Welch, P. D. 1967. The use of fast Fourier transform for the estimation of power spectra: A method based on time averaging over short, modified periodograms. *IEEE Trans. Audio Electroacoust.*, **AU-15**(2), 70–73.
- Xie, J., Ritzwoller, M. H., Shen, W., Yang, Y., Zheng, Y., and Zhou, L. 2013. Crustal radial anisotropy across Eastern Tibet and the Western Yangtze Craton. *J. Geophys. Res.*, **118**, 4226–4252.
- Xie, J., Ritzwoller, M. H., Shen, W., and Wang, W. 2017. Crustal anisotropy across eastern Tibet and surroundings modeled as a depth-dependent tilted hexagonally symmetric medium. *Geophys. J. Int.*, **209**, 466–491.
- Yang, Y., and Forsyth, D. W. 2008. Attenuation in the upper mantle beneath Southern California: Physical state of the lithosphere and asthenosphere. *J. Geophys. Res.*, **113**, B03308.
- Yang, Y., and Ritzwoller, M. H. 2008. Teleseismic surface wave tomography in the western U.S. using the Transportable Array component of USArray. *Geophys. Res. Lett.*, **35**, L04308.
- Yang, Y., Ritzwoller, M. H., Lin, F.-C., Moschetti, M. P., and Shapiro, N. M. 2008. Structure of the crust and uppermost mantle beneath the western United States revealed by ambient noise and earthquake tomography. *J. Geophys. Res.*, **113**, B12310.
- Yao, H., Gouédard, P., Collins, J. A., McGuire, J. J., and van der Hilst, R. D. 2011. Structure of young East Pacific Rise lithosphere from ambient noise correlation analysis of fundamental- and higher-mode Scholte-Rayleigh waves. *C. R. Geoscience*, **343**, 571–583.
- Zeng, X., and Ni, S. 2010. A persistent localized microseismic source near the Kyushu Island, Japan. *Geophys. Res. Lett.*, **37**, L24307.
- Zhang, J., and Yang, X. 2013. Extracting surface wave attenuation from seismic noise using correlation of the coda of correlation. *J. Geophys. Res.*, **118**, 2191–2205.
- Zheng, Y., Shen, W., Zhou, L., Yang, Y., Xie, Z., and Ritzwoller, M. H. 2011. Crust and uppermost mantle beneath the North China Craton, northeastern China, and the Sea of Japan from ambient noise tomography. *J. Geophys. Res.*, **116**, B12312.
- Zhou, L., Xie, J., Shen, W., Zheng, Y., Yang, Y., Shi, H., and Ritzwoller, M. H. 2012. The structure of the crust and uppermost mantle beneath South China from ambient noise and earthquake tomography. *Geophys. J. Int.*, **189**, 1565–1583.